Structure and dynamics of the Barents Sea Polar Front near the Great Bank and associated plankton distribution in August 2007

Selina Våge

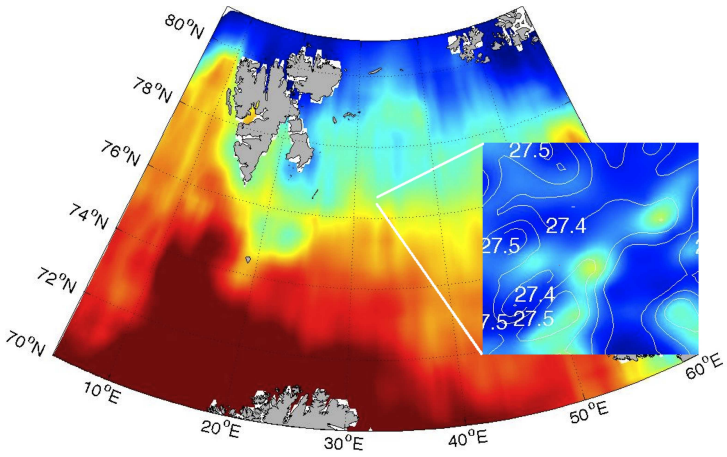

Master's Thesis in Biology - Field of Study Marine Ecology

(BIO-3950, 60 credits)

Department of Arctic and Marine Biology

Faculty of Biosciences, Fisheries and Economics

University of Tromsø

March 2010

"The payoff in increase
of knowledge often is
greatest the more
unconventional the
idea, especially when it
conflicts with collective
wisdom."

Henry Stommel

Abstract

The Polar Front separating Atlantic Water (AW) and Arctic Water (ArW) is one of the most dominant mesoscale features in the Barents Sea and a highly productive region. Here, the results of sub-mesoscale variability in physical and biological fields associated with the Barents Sea Polar Front (BSPF) at the Great Bank are reported from a high-resolution survey in August 2007. A nearly synoptic data set was collected using a ship-mounted Acoustic Doppler Current Profiler (ADCP) and an undulating instrument platform, equipped with a fluorometer, a Laser Optical Plankton Counter (LOPC) and Conductivity-Temperature-Depth (CTD) sensors. AW was found beneath ArW, leading to a surface and a deep expression of the front, which were shifted by about 40 kilometers and characterized by strong salinity and temperature gradients. Thermohaline compensation eliminated the cross-frontal density gradient at depth. The most dominant flow feature was a southeastward barotropic along-frontal jet with two cores at the surface and the deep expressions of the front. Tidal currents were negligible (estimated using the Arctic Ocean Inverse Tidal Model), while other ageostrophic processes retarded the frontal circulation and stimulated cross-frontal exchange. The hydrographic small scale structure of the front was highly patchy, presumably caused by turbulent stirring. The Arctic side of the front had a strong pycnocline, and the plankton community was in a post-bloom condition there. A summer phytoplankton bloom was observed on the Atlantic side, where nutrient upwelling was probably facilitated through shoaling isopycnals and a weaker pycnocline. Zoo- and phytoplankton occurred in small-scale patches that were correlated with the hydrographic small-scale variability.

Keywords: Barents Sea Polar Front; hydrography; currents; sub-mesoscale variability; patchiness; physical - biological interactions

Contents

List of Tables

List of Figures

1 Introduction

1.1 Oceanography of the Barents Sea

The Barents Sea is a relatively deep shelf sea with an average depth of 230 m (Loeng, 1991). The general flow pattern of the Barents Sea was described more than 400 years ago by Helland-Hansen & Nansen (1909). Atlantic Water (AW), Arctic Water (ArW) and Coastal Water are the three major water masses found in the Barents Sea, and they are associated with the three major current systems in the Barents Sea: the Atlantic Current, the Arctic Current and the Norwegian Coastal Current, respectively (Loeng, 1991). Tides and the bottom topography have a strong influence on the currents, in particular in the western Barents Sea (Berezutskii *et al.* , 1994; Kowalik & Proshutinsky, 1995; Løyning, 2001; Padman & Erofeeva, 2004; Ellingsen *et al.* , 2008), while variable amounts and properties of AW and ArW inflow lead to strong fluctuations of water temperature and ice cover (Sakshaug, 1997; Loeng *et al.* , 1997; Furevik, 2001; Ingvaldsen *et al.* , 2002; Hughes *et al.* , 2008).

The interface of the Atlantic and the Arctic Current forms the zone of the Barents Sea Polar Front (BSPF), which is the dominant mesoscale feature of the Barents Sea (Parsons *et al.* , 1996). An overview of the Barents Sea topography, the main currents, the mean frontal position of the BSPF and the study sections near the Great Bank is given in Figure 1.

1.2 Frontal circulation and the oceanic mesoscale

Fluid motion is fundamentally described by the Navier-Stokes equations, which arise from applying the continuity equation and Newton's second law to fluid motion (Cushman-Roisin, 1994). Assuming incompressibility (i.e. constant density ρ_0), the continuity equation can be expressed as

$$\frac{\delta u}{\delta x} + \frac{\delta v}{\delta y} + \frac{\delta w}{\delta z} = 0, \tag{1}$$

where (u, v, w) are the velocity components in the three spatial dimensions (x, y, z). For geophysical fluids, rotation strongly dominates other acceleration terms. Therefore, ignoring friction and assuming constant velocity and density, Newton's second law applied to geophysical fluids can be simplified to

$$\begin{aligned} -fv &= -\frac{1}{\rho_0}\frac{\delta p}{\delta x} \\ +fu &= -\frac{1}{\rho_0}\frac{\delta p}{\delta y} \\ 0 &= -\frac{1}{\rho_0}\frac{\delta p}{\delta z}, \end{aligned} \tag{2}$$

where ρ_0 is the density, p the pressure, and $f = 2\Omega sin(\phi)$ is the Coriolis parameter, where Ω is the Earth's angular velocity ($\approx 7.27{*}10^{-5}$ rad s^{-1}), and ϕ is the latitude. These simplified equations of continuity (1) and Newton's second law (2) predict a balance between the Coriolis and the pressure gradient forces. This is called geostrophic equilibrium, and dominates frontal circulation and most other geophysical flows (Cushman-Roisin, 1994).

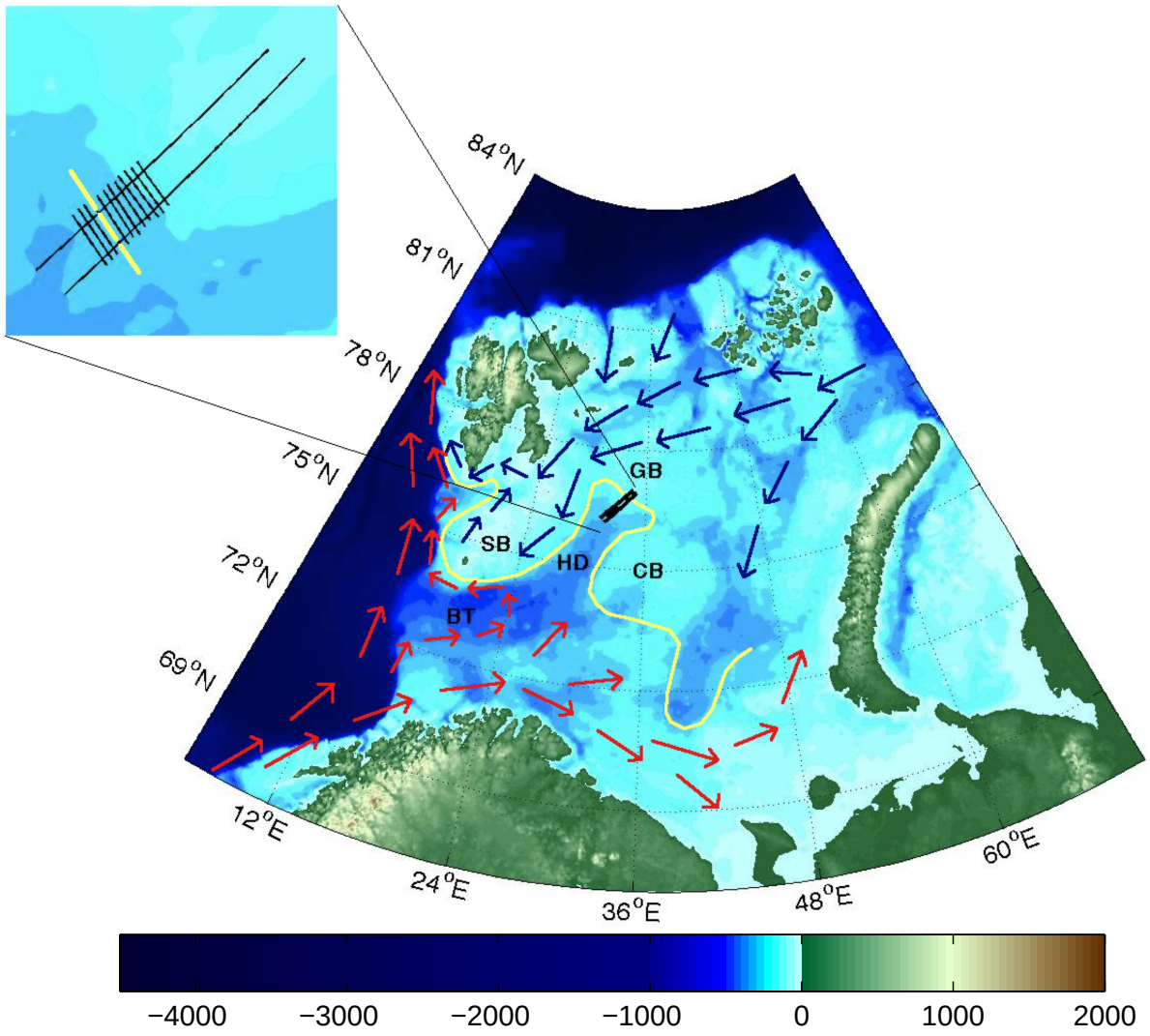

Figure 1: Map of the Barents Sea topography [m above sea level] based on the ETOPO2 data set. Warm and cold surface currents are shown in red and blue, respectively (adapted from Parsons *et al.*, 1996). The mean location of the BSPF is marked in yellow (adapted from Loeng, 1991). The blown up area shows the orientation of the BSPF relative to the sampling sections (black lines) in August 2007. The Bear Island Trough, the Spitzbergen Bank, the Hopen Deep, the Great Bank and the Central Bank are labeled with BT, SB, HD, GB and CB, respectively.

Solving the first two equations of (2) in terms of the velocity components u and v shows that the velocity vector (u, v) is perpendicular to the pressure gradient $(\delta p/\delta x, \delta p/\delta y)$. This means that the geostrophic flow follows the isobars, i.e. is isobaric. Also, inspection of the signs of the first two equations of (2) shows that the high pressure is to the right of the flow where f is positive, i.e. in the Northern Hemisphere.

The above statements are important to understand the frontal circulation in the present survey. Per definition, oceanic fronts separate distinct water masses, and close proximity of water masses with differing hydrographic properties often result in density and pressure gradients. Consequently, strong geostrophic jets typically occur along fronts.

Mesoscale meanders and eddies are commonly associated with frontal jets, and are also controlled by geostrophy (Cushman-Roisin, 1994; Rixen *et al.* , 2003a). Their lower bound is the internal Rossby radius of deformation

$$R_i = \frac{\sqrt{g'H}}{f}, \tag{3}$$

where $g' = g\frac{\Delta\rho}{\rho_0}$ is the reduced gravity, g the surface gravitational acceleration, $\Delta\rho$ the density difference between the two layers at the surface expression of the front, ρ_0 the mean density, H the depth of the upper layer, and f is the Coriolis parameter. R_i describes the typical length scale of frontal deformation. It is an expression of the distance that a disturbance can propagate until geostrophic balance is reached (Cushman-Roisin, 1994; Mann & Lazier, 2006). In the ocean, R_i is typically on the order of 5-50 km, depending on the latitude (Løyning, 2001; Robinson, 2006). The upper bound for the mesoscale can be defined as the distance at which mechanisms such as differential rotation (β-effect) become important besides geostrophy (Robinson, 2006).

In addition to the dominant geostrophic flow, secondary ageostrophic circulation is typical in fronts. This includes cross-frontal circulation and subduction of the denser water mass under the lighter water mass, which are important mechanisms for water mass formation through mixing (Nagai *et al.* , 2008). Furthermore, upwelling of nutrients into the euphotic zone through ageostrophic processes is an important mechanism controlling phytoplankton blooms near fronts (Nagai *et al.* , 2008; Rixen *et al.* , 2003b; Garcia *et al.* , 2008).

Fronts have become an area of high interest in the oceanographic community, as they are now understood to be important for both global dynamical systems such as the climate, and regional productivity. For example, oceanic mesoscale processes, including fronts, account for most of the energy transfer in the open ocean (Rixen *et al.* , 2003a, and references therein). It has been shown that the resolution of 2° and lower commonly used in coupled ocean-atomosphere climate models leads to an underestimate of the poleward heat transport due to inadequate resolution of mesoscale processes (Fanning & Weaer, 1997). Moreover, regional primary production increased when a resolution sufficient to simulate oceanic mesoscale variability was used in a physical-biological coupled model system (Hansen & Samuelsen, 2009). Field surveys of the oceanic meso-

and sub-mesoscale variability, such as the one presented here, are therefore important to gain a better understanding of these processes, which must be represented more accurately by the climate models.

1.3 Barents Sea Polar Front

Since the BSPF is the dominant mesoscale feature in the Barents Sea, many studies have focused on the front (Harris *et al.* , 1998). It is known for the formation of Polar Front Water (PFW) through mixing of AW and ArW and considered the southern boundary of sea ice (Loeng, 1991; Gawarkiewicz & Plueddemann, 1995; Harris *et al.* , 1998).

Johanessen & Foster (1978) were among the first scientists to describe the BSPF using observations that were made in the summer of 1974. They determined the location of the front using a temperature gradient criterion, reaching up to 0.5°C km^{-1} across the front, which occurred between the 3 and 4°C isotherms. The gradient streched from Svalbard in the north to the south of Bear Island, from where it made a northward loop far into the Barens Sea before turning southward again, covering a distance of roughly 1500 km in total. This path is consistent with the mean frontal position shown in Figure 1 (Loeng, 1991). A topographic control of the front was also found, with the BSPF generally following the 100-m isobath (Johannessen & Foster, 1978). Later studies confirmed the topographic control by showing that the BSPF is strongly confined by the bottom topography on the southern flank of the Spitzbergen Bank, although the front follows approximately the 250 m isobath there, while windy conditions can move it further upslope (Gawarkiewicz & Plueddemann, 1995; Harris *et al.* , 1998; Ingvaldsen, 2005).

Due to its higher density, AW submerges beneath ArW in the frontal region (Sakshaug & Slagstad, 1992). In the western half of the Barents Sea, the BSPF is well defined, whereas it is a broader zone of mixing in the east (Loeng, 1991). At the Great Bank, mixing and local water mass formation is thought to occur through tidal dynamics and salinization (Løyning, 2001).

Hydrographic and flow properties of the BSPF were investigated at high resolution (2.5 km) east of Bear Island in the summer of 1992 by Parsons *et al.* (1996). They detected a strong surface front with nearly horizontal isopycnals and a weaker front below 100 m. The horizontal scale of the front was found to be approximately 3 km, while strong M2 and S2 tidal signals caused significant lateral variation of the front.

A strong correlation between the hydrographic and flow characteristics of the front was observed in the southern Barents Sea (Berezutskii *et al.* , 1994). However, rapidly evolving ageostrophic phenomena were also detected based on an incomplete correspondence between the hydrographic and acoustic properties of the front (Berezutskii *et al.* , 1994). The occurrence of ageostrophic processes in the BSPF was confirmed by Harris *et al.* (1998). They showed that fresh surface water crossed the front from the Spitzbergen Bank to the southern side of the front in the summers of 1991 and 1993, but did not provide a dynamical explanation.

Despite cross-frontal exchange taking place, the

BSPF imposes a biogeographical boundary for certain zooplankton and fish species, and it is important for the overall distribution of productivity in the Barents Sea (van Aken *et al.* , 1991; Sakshaug & Slagstad, 1992; Johansen, 2002; Loeng & Drinkwater, 2007). New production is estimated to be twice as high to the south of the front compared to the northern side, while the actual frontal zone is highly productive (Sakshaug & Slagstad, 1992; Sakshaug, 1997). It is therefore an important grazing area for commercially important fish species (Mehlum *et al.* , 1998; Munch, 2008; Dalpadado & Bogstad, 2004). Productivity might be enhanced by the hydrographic and dynamical sub-mesoscale characteristics of the BSPF, which motivates the presented study besides its contribution to a more fundamental physical understanding of the BSPF.

1.4 About this study

Most previous studies of the BSPF were based on data with relatively low spatial and temporal resolution, which consequently only permitted a coarse description of the front. Moreover, many BSPF studies were conducted in the western Barents Sea, where the front is most pronounced. The purpose of this study is, firstly, to provide a description of the hydrographic and dynamical structure of the BSPF on the southwestern flank of the Great Bank, and to compare this with former investigations on the BSPF. Secondly, a novel description of the physical sub-mesoscale structure and dynamics of the BSPF will be given using a high-resolution three-dimensional data set. As a supplement, the biological structure of the BSPF near the Great Bank will be presented and discussed in the light of the physical findings of this study.

2 Data and Methods

2.1 Field program and measurement devices

The data used in this study were collected in connection with the Norwegian component of the 2007-2008 International Polar Year (IPY) project *Ecosystem Studies of Subarctic and Arctic Regions* (NESSAR). NESSAR focused on frontal zones and the effect of climate variability on the ecosystems in the Barents and Norwegian Seas. The cruise was conducted on the Hopen Bank and the Great Bank from July 30 to August 18, 2007, on the RV *Jan Mayen*. Relevant data for this study were solely collected on the southwestern flank of the Great Bank between about 76 - 77°N and 31 - 35°E (Figure 2).

The survey was conducted using a ship-mounted 76.8 kHz Broad Band Ocean Surveyor Acoustic Doppler Current Profiler (ADCP, Teledyne RD Instruments, CA, USA) and an undulating, towed instrument platform (Scanfish, MacArtney Inc. Esbjerg, Denmark) equipped with a fluorometer (Seapoint Chlorophyll Fluorometer, Seapoint Sensors Inc., NH, USA), a Laser Optical Plankton Counter (LOPC, Brooke Ocean Technologies, NS, Canada) and SBE911 plus Conductivity-Temperature-Depth sensors (CTD, Sea-Bird Electronics, WA, USA). Two long cross-frontal sections (sections 20 and 22, 119 and 125 km

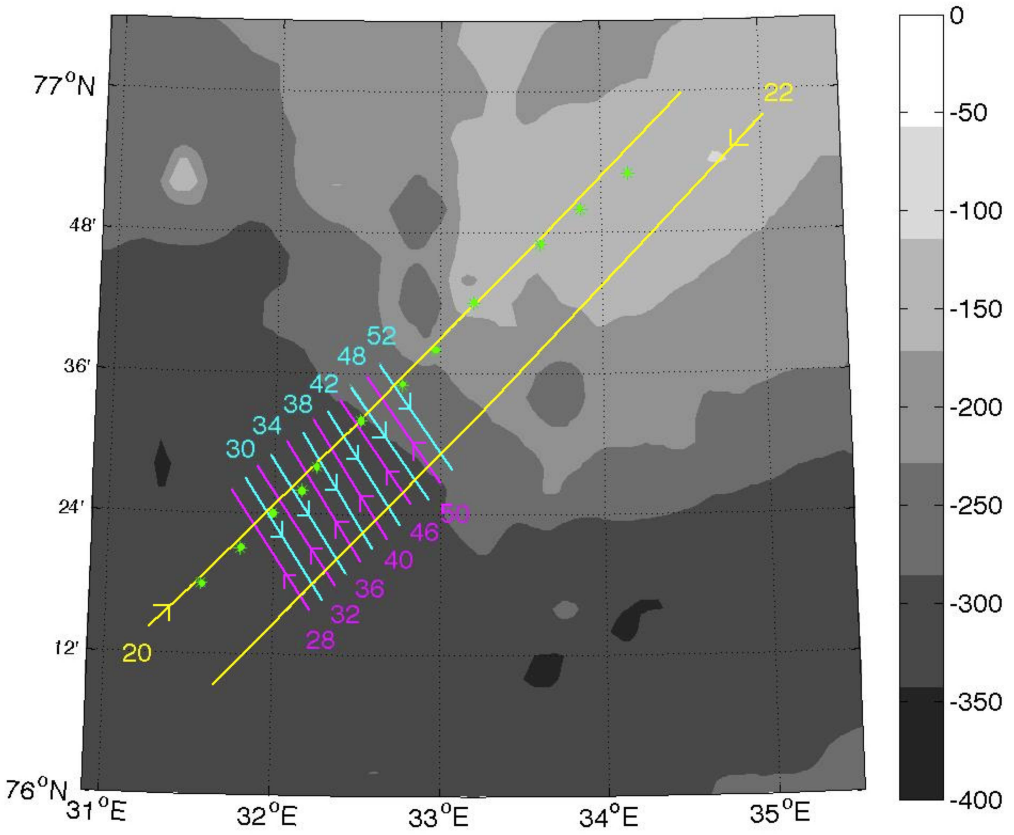

Figure 2: Sampling sections for ship-mounted ADCP and Scanfish instrument platform (colored lines) and full-depth CTD stations (green dots). The sampling direction for each section is indicated with an arrow.

Table 1: Ship-mounted ADCP and Scanfish sampling sections. Note that the Scanfish instrument platform only reached a maximal depth of 75 m, while the ADCP recorded velocities in the entire water column.

No.	Start position °E, °N	End positon °E, °N	Length km	Max. depth m	Sampling duration UTC
20	31.27, 76.24	34.50, 77.00	118.53	305	08.08.07 07:43-16:58
22	35.01, 76.96	31.66, 76.16	124.58	297	08.-09.08.07 18:10-03:52
28	32.22, 76.26	31.75, 76.43	22.29	261	13.08.07 14:21-16:13
30	31.82, 76.45	32.29, 76.28	22.53	255	13.08.07 16:28-18:14
32	32.37, 76.30	31.90, 76.47	22.28	246	13.08.07 18:36-20:24
34	31.98, 76.48	32.43, 76.32	21.71	247	13.08.07 20:41-22:25
36	32.52, 76.33	32.08, 76.50	21.54	242	13.-14.08.07 22:46-00:30
38	32.16, 76.52	32.58, 76.36	20.53	240	14.08.07 00:51-02:30
40	32.68, 76.37	32.22, 76.54	22.24	240	14.08.09 02:48-04:34
42	32.32, 76.55	32.74, 76.39	20.33	240	14.08.07 04:52-06:32
46	32.82, 76.42	32.37, 76.57	20.33	230	14.08.07 07:06-08:41
48	32.45, 76.58	32.92, 76.43	21.53	227	14.08.07 09:00-10:44
50	33.00, 76.44	32.55, 76.59	20.54	220	14.08.07 11:02-12:40
52	32.63, 76.61	33.06, 76.47	19.87	213	14.08.07 12:58-14:30

long, respectively) and twelve short sections parallel to the front (sections 28 to 52, 20-23 km each) were sampled (Figure 2, Table 1). Data from the twelve short along-frontal sections are assumed to be representative of a synoptic survey, although true synopticity could not be achieved as the sampling required about 24 hours between August 13 and August 14, 2007 (Table 1). The two long cross-frontal sections were sampled within 20 hours between August 8 and August 9, 2007 (Table 1). The ADCP was set to collect data through the entire water column (max. depth 305 m), while the Scanfish platform was towed in the upper 75 m to resolve the horizontal structure of the surface front. The sampling volume covered by the towed Scanfish platform in the twelve short sections will be referred to as the High-Resolution-Sampling-Volume (HRSV). The HRSV was roughly 22 x 50 km wide and 75 m deep, with a horizontal resolution of 2 km and higher. Additionally to the sections, twelve full-depth CTD stations with a spacing of about 5-10 km were conducted along section 20 between August 14 and August 15, using a Sea-Bird SBE911 plus CTD profiler (green dots in Figure 2, Table 2). Wind speed and direction were measured on board with a WindObserver II instrument (Gill Instruments Ltd, England).

2.2 ADCP settings, data processing and final products

ADCP recording

The ADCP continuously recorded current vectors while underway. The bin length was set to 16 m and the transducer depth was 7 m. 20 bins were measured in the vertical, giving the ADCP a nominal range between 23 m and 327 m, while the bottom was never deeper than 305 m. Four beams (ping) with a frequency of 76.8 kHz were emitted simultaneously at a rate of one ping per second. While underway, bin velocities relative to the transducer were calculated from the backscattered signal's Doppler shift. WinADCP software version 1.13 from RD Instruments was used to transform the raw ADCP data into a Matlab readable format. Matlab version R2008a from MathWorks was used to further process and visualize all data.

Table 2: Full depth CTD stations. The stations are listed from northeast to southwest.

Position °E, °N	Depth m	Time UTC
32.17, 76.88	138	14.08. 19:06
32.87, 76.83	117	14.08. 22:34
32.62, 76.78	102	15.08. 00:37
32.20, 76.70	159	15.08. 02:31
32.97, 76.63	193	15.08. 04:07
32.77, 76.58	243	15.08. 05:47
32.52, 76.53	249	15.08. 07:30
32.25, 76.47	267	15.08. 10:10
32.17, 76.43	273	15.08. 12:18
31.98, 76.40	374	15.08. 13.39
31.57, 76.30	318	15.08. 16:08
31.80, 76.36	300	15.08. 18:39

ADCP time average and ship speed removal

As the ADCP system's internal gyro compass malfunctioned during the survey, independent geographical positioning system (GPS) data were used to determine the position of each velocity profile. This was done by matching the times from the GPS data with the ADCP ensemble recording times (time accuracy of one minute). Five-minute ensemble averages

(long term average, LTA) were used to reduce the error. LTA more than halved the error compared to one-minute averaged profiles, to approximately 0.03 m s^{-1}.

The LTA raw data consisted of series and bottom track (BT) data. The series raw data contained horizontal water velocities relative to the ship for all bins (along-track velocities u' and cross-track velocities v'). The BT data had only one bin at the bottom, in which the along- and cross-track velocity components represent the horizontal velocity of the ship relative to the bottom (Trump & Marmorino, 1998). To remove the ship speed from the measured series velocities, the BT along- and cross-track velocities were added to the series along- and cross-track velocities, respectively.

ADCP data filtering

Data with error velocities higher than 1 m s^{-1} were removed at first. The threshold was chosen from examination of scatter-plots of absolute error velocities for each section (not shown). A few outliers had error velocities well in excess of 1 m s^{-1}, while the vast majority of the data points had error velocities below 1 m s^{-1}. Data from the first bin and from the zone above the bottom, which made up 15 % of the distance between the transducer and the bottom, were discarded, as they are known to contain significant amounts of ringing noise and erroneous bottom signals. After removal of the outliers and the boundary data, a filter was applied to remove data outside the range of ± two standard deviations (sd) from the mean velocity in each section. Along-track velocity components were still significantly contaminated with suspiciously high velocities close to 1 m s^{-1} after the 2-sd filter had been applied (not shown). Therefore, a final filter was applied to remove all data with velocities higher than 50 cm s^{-1}. This threshold was assumed to be an upper limit for the current speed near the BSPF based on Berezutskii *et al.* (1994).

North-east transformation

Due to the malfunction of the internal navigation function (gyro compass), no accurate information about the heading, the pitch and the roll of the ship during the survey is known. Without the heading information, the necessary angle γ (Figure 3) to transform the velocity components automatically into east-north components during the data logging was not available. For the purpose of interpolating the horizontal velocity fields, the along- and cross-track components of the twelve short sections were therefore transformed into the Earth coordinate system (E, N) during the processing phase. The coordinate systems and angles used for this transformation are shown in Figure 3. Note that the misalignment angle λ (2.15° in this survey) was taken into account while logging the data, such that the along- and cross-track velocity components in the raw data were given in the ship's coordinate system (X,Y) instead of the transducer's coordinate system (X', Y').

For the transformation, it was necessary to assume that the heading (the direction of the major ship axis) and the crossing (the direction in which the ship was moving) were equal during the survey. This is a potential source of error, since the surface currents were relatively strong along the front. For each section, a

straight line was fitted through all of the ensemble positions. From this line, the starting and end positions of the section were determined. The angle γ was then computed. For the sections that were sampled from roughly southeast to northwest (e.g. section 28, 32, etc., Figure 2), this resulted in an angle γ of approximately 125°, while it gave an angle of about -56° for the remaining short sections (sampled from roughly northwest to southeast). The exact value for γ varied for each section. The eastern (u) and northern (v) velocity components for each section were finally computed as follows:

$$u = u'_{BT}cos(\gamma) - v'_{BT}sin(\gamma) \quad (4)$$
$$v = u'_{BT}sin(\gamma) + v'_{BT}cos(\gamma),$$

where u'_{BT} and v'_{BT} are the horizontal along- and cross-track velocity components, respectively, after adding the BT velocities (Fong & Monismith, 2004).

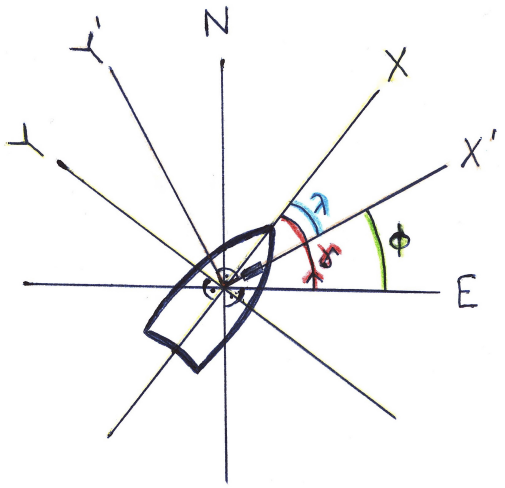

Figure 3: Coordinate axes and angles used to transform the along- and cross-track velocity components into east-north components. The transducer is sketched as a black box on the X'-axis.

Tidal currents

The Arctic Ocean Tidal Inverse Model (AOTIM5, Padman & Erofeeva, 2004) was used to remove the tidal currents from the data by subtraction of model outputs from the north-east transformed ADCP currents. AOTIM5 is a high-resolution (5 km regular grid) model for barotropic tides in the Arctic Ocean (Figure 4), and calculates 8 tidal constituents.

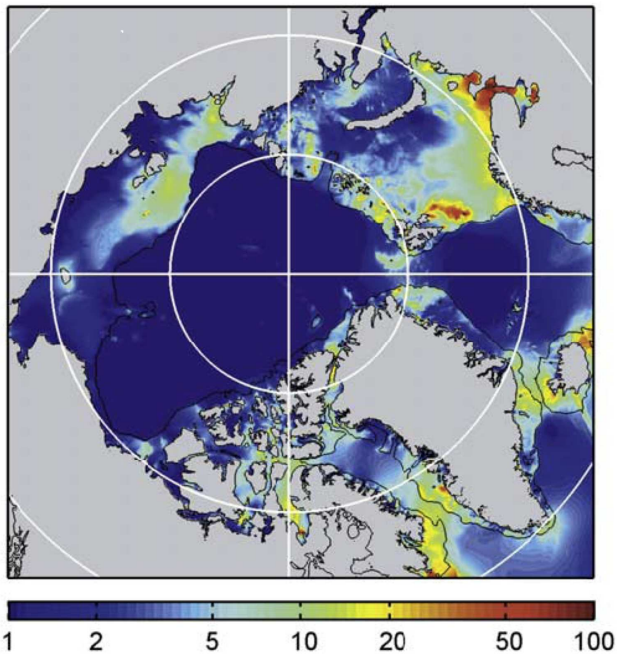

Figure 4: Model domain and mean tidal current speed [cm s^{-1}] from simulation of hourly tidal velocities over a period of 14 days using AOTIM5 (from Padman & Erofeeva, 2004).

Interpolation

To plot horizontal current fields, an objective analysis (OA) interpolation method based on Bretherton *et al.* (1976) and Dorland & Zhou (2008) was used to fit a 2-dimensional non-diverging streamline function

onto the horizontal ADCP current measurements. OA is based on the Gauss-Markov theorem, which states that if the covariance function used in the Gauss-Markov mapping is the covariance of the actual data field, then the Guass-Markov smoothing is optimal in the sense that it minimizes the mean square error of the objective estimates (Emery & Thomson, 2004). The optimal estimator is linear and consists of a weighted sum of all the observations within a specified range surrounding each grid point. OA relies on two fundamental assumptions. Firstly, that the statistics of the data field are stationary over the sampling period, and secondly, that the statistics are homogenous over the entire data field (Emery & Thomson, 2004). The OA statistics used in this study were the decorrelation length scales in the eastern and northern directions and the covariance function. Decorrelation scales of 15 km in the eastern and northern directions were chosen (see subsection 4.1 for the justification). The distance between each grid point was approximately 1.2 km, and the 50 nearest data points were used to interpolate the optimal value for each grid point. The covariance function

$$(1 - r^2)e^{-r^2}$$

was used, where r denotes the distance between two spatial points.

Cross-sectional velocity components as well as hydrographic and planktonic data were interpolated using linear Delauny triangulation (D'Ericco, 2006), where the vertical and horizontal grid resolution was between 1-10 m and 1-2 km, respectively. A consistent sign convention was chosen such that positive cross-sectional velocity components come out of the page throughout this thesis.

2.3 Towed instruments

2.3.1 Scanfish towing and data resolution

The towed Scanfish instrument platform was used to obtain nearly continuous hydrographic and biological measurements, resulting in a high-resolution survey of the spatial variability in the surface expression of the BSPF. Real-time GPS data were merged with the Scanfish recordings during the logging. The ship speed was approximately 7 knots ($\approx$ 3.5 m s^{-1}), while the Scanfish platform was undulating between 2-3 m below the surface and 75 m, logging hydrographic and planktonic data twice every second. The depth range was chosen to include the mixed layer (which was shallower than 30 m) and to fully cover the surface expression of the front. The horizontal and vertical scales of the surface front were about 20 km and 50 m, respectively, which were covered by the twelve short sections in 24 hours when restricting the sampling depth to 75 m. The spacing between the short sections was about 2 km, while the two long sections were about 12 km apart (Figure 2). The undulating motion of the Scanfish platform resulted in a horizontal resolution of 0-1.7 km for the hydrographic and planktonic data within each section at a given depth level. At the twelve full-depth stations, CTD data were recorded at an interval of 1 decibar [db], giving a vertical resolution of approximately 1 m.

2.3.2 CTD data processing and final products

Salinity [psu] was inferred from the measured conductivity while underway. Distances, potential temperatures (θ, reference pressure 0 db), potential densities (ρ, reference pressure 0 db), geopotential anomalies, geostrophic currents as well as the thermal expansion and the saline contraction coefficient were computed from the CTD data using the the Matlab CSIRO *Seawater* package (Version 3.2, `http://www.cmar.csiro.au/datacentre/ext_docs/seawater.htm`). 1000 kg m^{-3} was subtracted from all potential densities to obtain $\sigma_\theta = \rho(\theta, S, 0) -$ 1000 kg m^{-3}.

CTD data filtering

Occasional CTD data with erroneous coordinates were removed at first. The mean and standard deviation (sd) of CTD data that were consecutively recorded within 1 m vertical depth at a given position were then computed. Data points lying outside ± 2-sd from the mean were removed and the new mean was computed, which was used for the remaining analysis.

Computation of the internal Rossby radius of deformation and the horizontal density ratio

The internal Rossby radius of deformation (R_i) was computed using formula (3).

To determine the importance of salinity and temperature for the horizontal density gradient near the surface of the front, the dimensionless horizontal density ratio D_x, as described in May & Kelley (2002), was computed as

$$D_x = \frac{\alpha\theta_x}{\beta S_x}, \tag{5}$$

where α is the thermal expansion coefficient for seawater (describing the change in volume with temperature), β the haline contraction coefficient (describing the change in volume with salinity), and θ_x and S_x are the horizontal θ and salinity gradients in °C m^{-1} and psu m^{-1}, respectively. β and α were computed for θ = 5°C and salinity = 34.9 psu at sea surface pressure.

Computation of geostrophic currents

Geostrophic currents perpendicular to the sections were computed based on the density field and the thermal wind relation (Pedlosky, 1996). The CTD data were interpolated onto 50 horizontal grid points along each section. For the two long sections, this gave a horizontal resolution of approximately 2.4 km, which is similar to the distance between the short perpendicular sections (Figure 2). The horizontal density gradients between two neighboring grid points and the resulting vertical velocity shear were then computed (Morgan, 1994). To obtain the absolute geostrophic currents, the ADCP current measurements at 70 m were chosen as the reference currents. The ADCP currents at 70 m are deep enough to avoid ringing associated with the ADCP mounting and have high signal to noise ratios. At the chosen horizontal resolution, three ensemble velocity means were averaged to further reduce measurement errors.

2.3.3 LOPC and fluorometer settings and data processing

The towed LOPC recorded particles between approximately 0.1 and 35 mm estimated spherical diameter [ESD] using a laser and precision optics, which detected particles transiting through the sampling tunnel (Herman *et al.* , 2004). The fluorometer recorded the relative phytoplankton standing crops by measuring emitted fluorescent light from chlorophyll-a, after the chlorophyll was exposed to an excitation filter (Miller, 2004).

The quality of the LOPC data was controlled by plotting the size of all recorded particles for each section. Particles that were smaller than 250 μm ESD were excluded from further analysis as small ESD are known to have a low signal to noise ratio. For the purpose of this study, the LOPC particle counts between 250 μm and 3.8 mm ESD (largest particle recorded in this study) were summed. Fluorescence and zooplankton abundances were averaged over a depth interval of 1 m. The 2-sd filter applied to the CTD data was not used, since plankton distributions are often patchy on small scales. Such small-scale variability could be missed with additional smoothing.

2.4 External data bases

Sea surface temperature (SST) fields for August 15, 2007, were obtained from the daily satellite SST database provided by NOAA's National Climate Data Center (`http://www.ncdc.noaa.gov/oa/climate/research/sst/oi-daily.php`). The ETOPO2 database (2-minute horizontal resolution) from the National Oceanic and Atmospheric Administration (NOAA, Boulder, CO, USA, `http://www.sos.noaa.gov/datasets/Land/etopo2.html`) and the Matlab package *m_map* (version 1.3, `http://www.eos.ubc.ca/~rich/map.html`) were used to plot the topographic maps of the Barents Sea.

3 Results

3.1 Quality of raw versus processed data

Hydrographic and biological data

The hydrographic and planktonic data proved to be of high quality. No density inversions were found in the CTD data, and they showed the expected structure of the front.

The size distribution of the LOPC data typically showed a normal distribution with a mean of about 400 μm ESD and a tail extending towards large particles (Figure 5). No obvious outliers were found except for the size class below 250 μm ESD, which is known to contain a high level of noise.

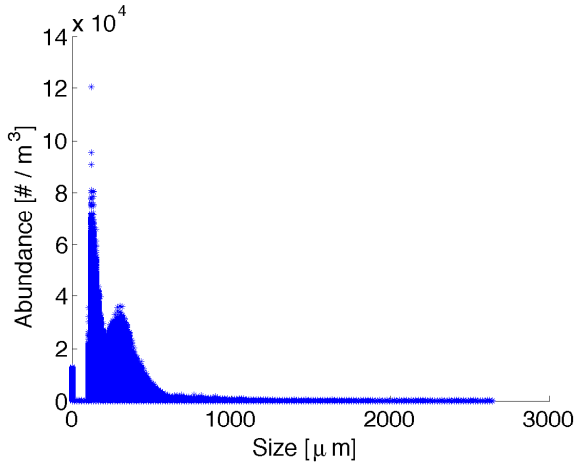

Figure 5: Zooplankton size distribution in section 28 as a representative example for all other sections. Noise is visible below 250 μm ESD.

ADCP data

In contrast to the hydrographic and planktonic data, the raw current data were of relatively poor quality prior to the processing. In particular, the %-good numbers were very low for three of the four beams in all sections (Figure 6). In the following, the quality of the raw and processed ADCP data is illustrated using data from sections 28 and 20, which are representative examples for the short and long sections, respectively.

The raw along-track components in section 28 had a much higher variance than the cross-track components (Figure 7, top left, shown in red). Error velocities were relatively low for bin 2 through bin 14, where most values were around $\pm$ 5 cm s^{-1} (top middle of Figure 7). Signal echo amplitudes were very similar for the four beams (not shown). The mean echo amplitude in the raw data of section 28 decreased rapidly close to the surface, followed by a more slow decrease with depth. Near bin 14, the mean echo amplitude increased suddenly due to the presence of the bottom (Figure 7, top right).

After the processing, the along- and cross-track components in section 28 had a similar variance and were centered around values close to 0 cm s^{-1} (Figure 7, bottom left). The error velocities were exclusively less than 10 cm s^{-1} in absolute value after the processing, and the mean echo amplitude logarithmically decreased with depth, as expected (Figure 7, bottom middle and right, respectively). The %-good values of the processed data, on the other hand, remained low for beam 1 through beam 3 (not shown).

Raw data from sections 20 and 22 were similar in terms of quality as described above for the short sections, although some additional noise from an unknown source was present (Figure 8, top row). This included occasional extreme along-track velocities near -32 m s^{-1} and mean echo amplitudes with unnaturally large peaks towards the right (Figure 8, top left and right, respectively). The processing procedure used was not sufficient to completely remove the high variance in the along-track components and the erroneous echo amplitude profiles (Figure 8, middle row). These irregularities would only have disappeared after application of a third, more rigorous filter, which consisted of removing all data with error velocities higher than 3 cm s^{-1}. This third filter was not applied as its effect was not qualitatively visible in the interpolated fields of the cross-sectional currents (not shown). Also, it would have caused an unnecessary loss of valid data in the short along-frontal sections.

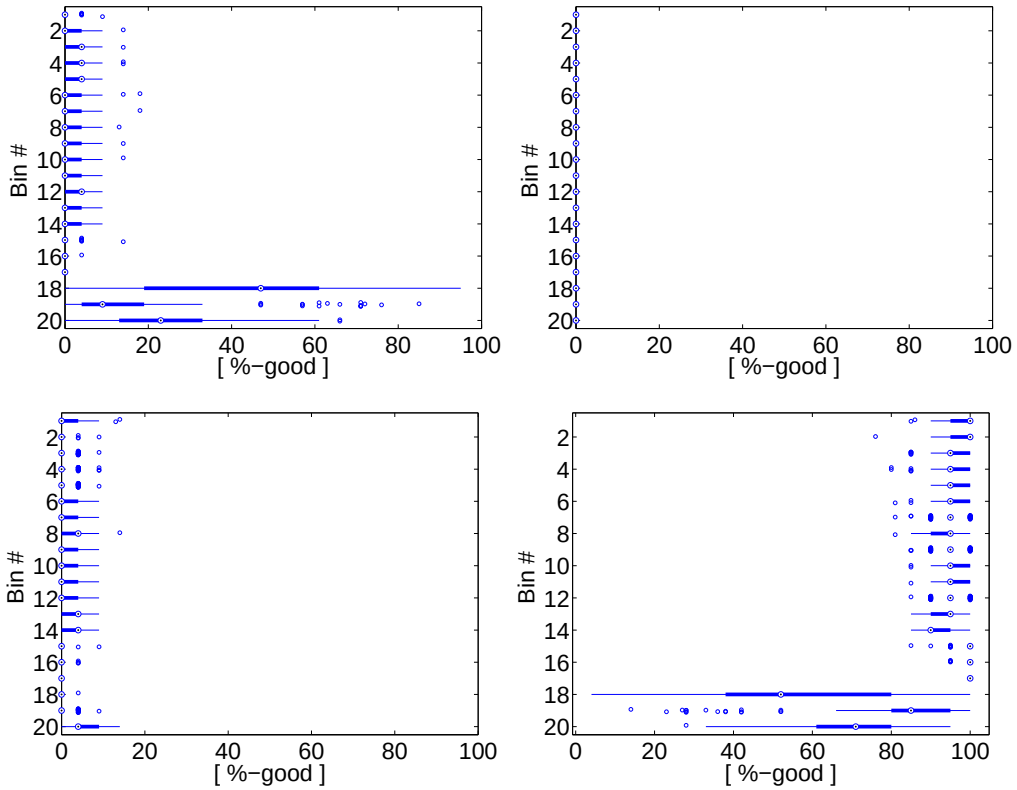

Figure 6: Box-plots with %-good values for beam 1 (*top left*) through beam 4 (*bottom right*). Data from section 28 are shown as a representative example for all other sections. Medians are shown as a white circles with a central dot, ranges between the lower and the upper quartile are shown as solid lines, and outliers are marked as white circles.

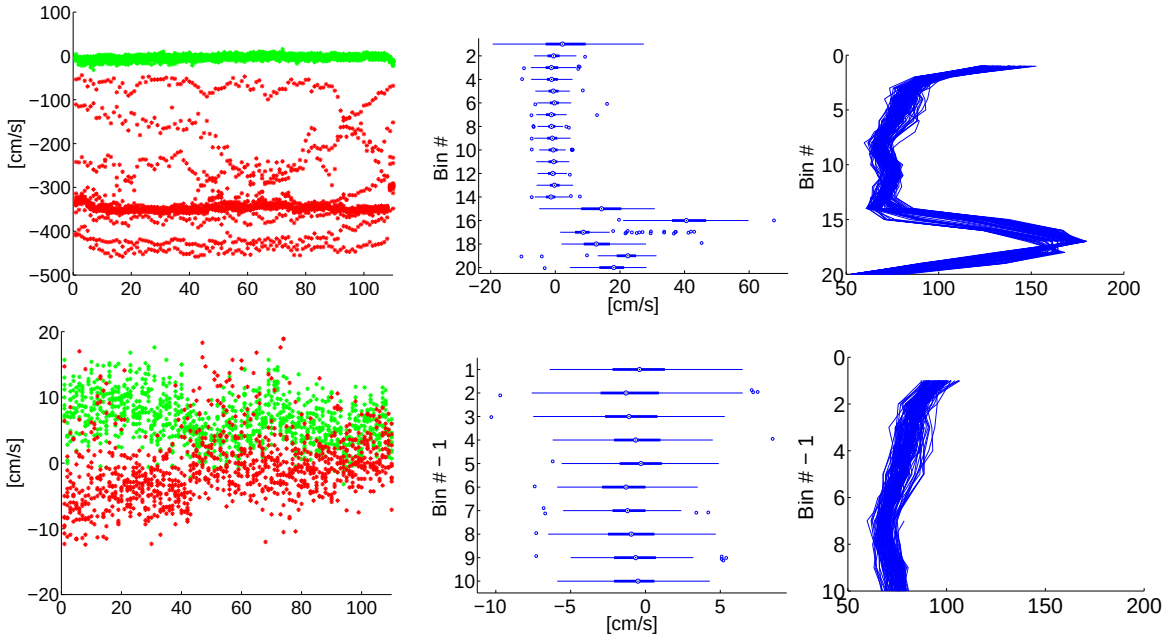

Figure 7: Along- (red) and cross-track (green) velocity components (*left*), error velocities (*middle*, box-plot explanations as in Figure 6) and mean echo amplitudes (*right*) in section 28 for raw data (*top*) and processed data (*bottom*). Note the different x-axes scales for the error velocities in the central column. The centering of the raw along-track components around - 3.5 m s^{-1} comes from the ship speed.

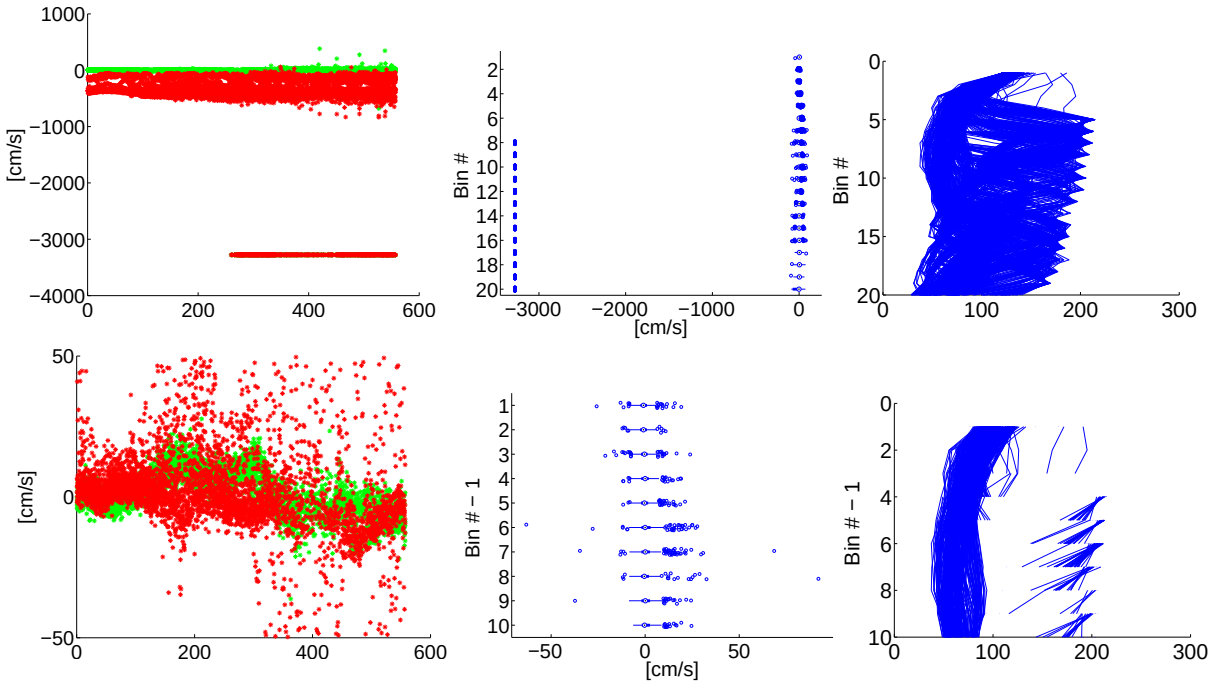

Figure 8: As Figure 7, but using data from section 20.

3.2 Hydrography

Sea surface temperatures in the Barents Sea

In August 2007, the southern Barents Sea was dominated by relatively warm water with an SST around 10°C (Figure 9, top). This water was of Atlantic origin and is known to enter the Barents Sea from the Norwegian Sea along the northern coast of Norway (Loeng, 1991). In the north, at the border between the Barents Sea and the Arctic Ocean, the SST was around 0°C. This cold water enters the Barents Sea from the Arctic ocean between Svalbard and Franz Joseph Land and between Franz Joseph Land and Novaya Zemlya (Ingvaldsen & Loeng, 2009). The surface water directly south of the study area was between 6 and 8°C, while the SST directly north of it was around 4°C (Figure 9, top). The white zone in the top of Figure 9 shows the extent of dense sea ice cover.

The SST gradient in the Barents Sea was strongest near the 6° isotherm in the western Barents Sea, south of the Spitzbergen Bank (Figure 9, top). This marks the area where the BSPF was most pronounced. Towards the east, starting near the Great Bank, the surface of the BSPF became wider and the temperature gradient across the front weaker (Figure 9, top and bottom left). The broadening of the frontal zone east of the Great Bank was also accompanied by an increased mismatch between the bottom topography and the SST gradient. This was expressed in the easterly continuation of the isotherms instead of a southward turn of the front to follow the Hopen Deep bathymetry (Figure 9, bottom left).

Hydrography across the Polar Front at the southwestern flank of the Great Bank

Data from the CTD stations across the BSPF showed that water of Atlantic origin was submerged beneath a surface layer of Arctic origin, which led to a surface and a deep expression of the front (Figure 10). The surface expression of the front was located approximately above the 275 m isobath, while the deep expression reached the bathymetry of the Great Bank near the 125 m isobath. The two frontal expressions were shifted by about 40 km, and characterized by strong salinity and temperature gradients. The gradients were strongest over a horizontal distance of about 15 km in the surface and deep expressions of the front (Figure 10).

The mixed layer depth (defined as the depth of the surface layer with homogenous θ) was about 25 m on the Atlantic side of the front and 15 m on the Arctic side (Figures 10 and 11). The horizontal salinity gradient was strongest in the top 20 m of the surface front, i.e. within the mixed layer, with salinities of 35 psu on the Atlantic and 34.6 psu on the Arctic sides (Figure 10, top). This caused a salinity gradient of roughly 0.4 psu over 15 km, or 0.03 psu km^{-1} across the surface expression of the front. Below 70 m, where the deep expression of the front was located, the salinity gradient was only about 0.25 psu over 15 km, or 0.02 psu km^{-1} (35 psu on the Atlantic side and 34.75 psu on the Arctic side).

In the mixed layer, the horizontal temperature gradient was strongest between the 5 and 6°C isotherms, amounting to a gradient of about 1°C over 15 km, or 0.07°C km^{-1} (Figure 10, bottom). This confirms

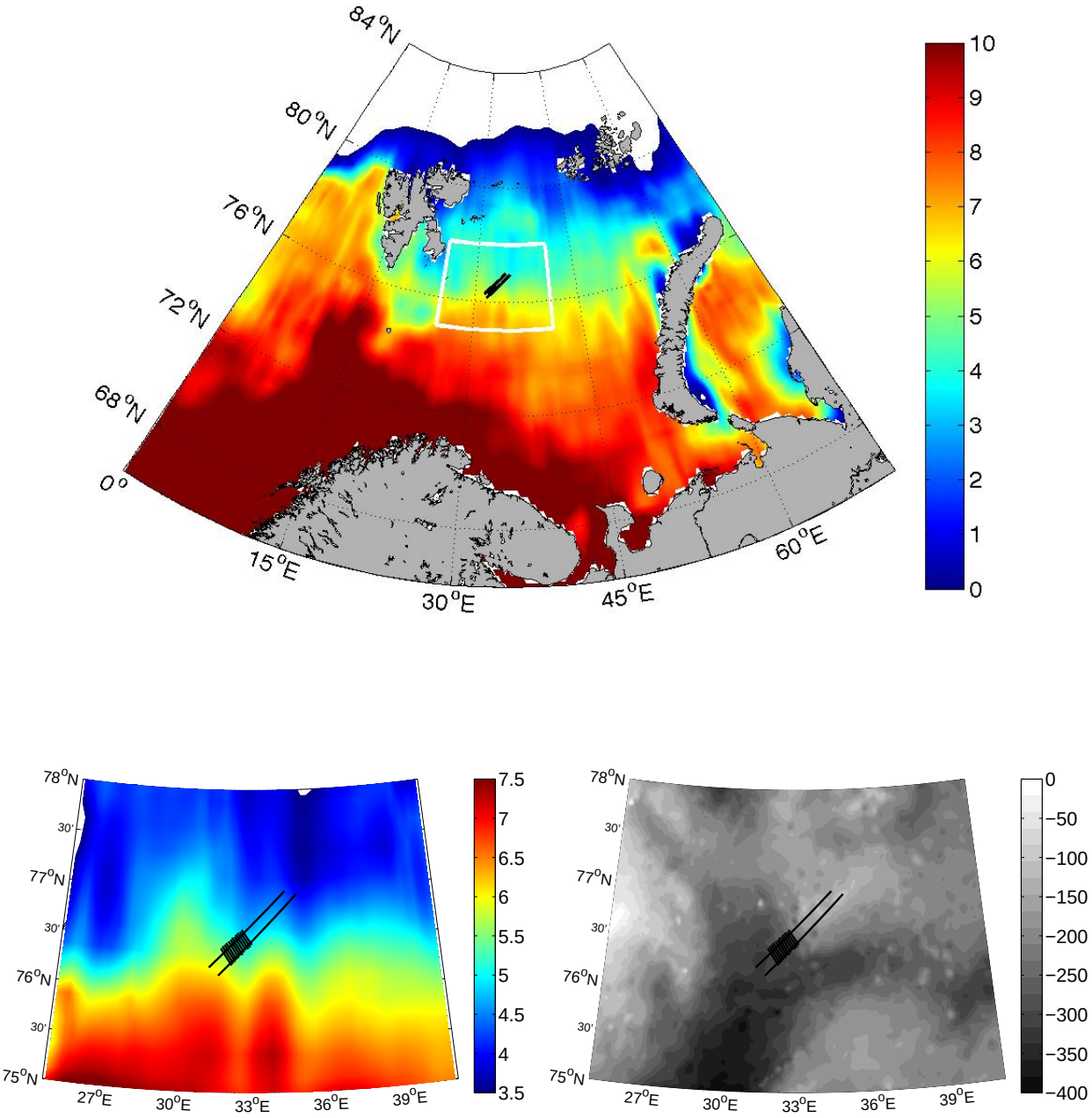

Figure 9: *Top* and *bottom left*: SSTs [°C] of the Barents Sea on August 15, 2007. Note the different SST colorbar scales. *Bottom right*: Bathymetry near the survey region [m above sea level]. The sampling sections are marked by the black lines. The area of the lower subfigures is indicated by the white box on top.

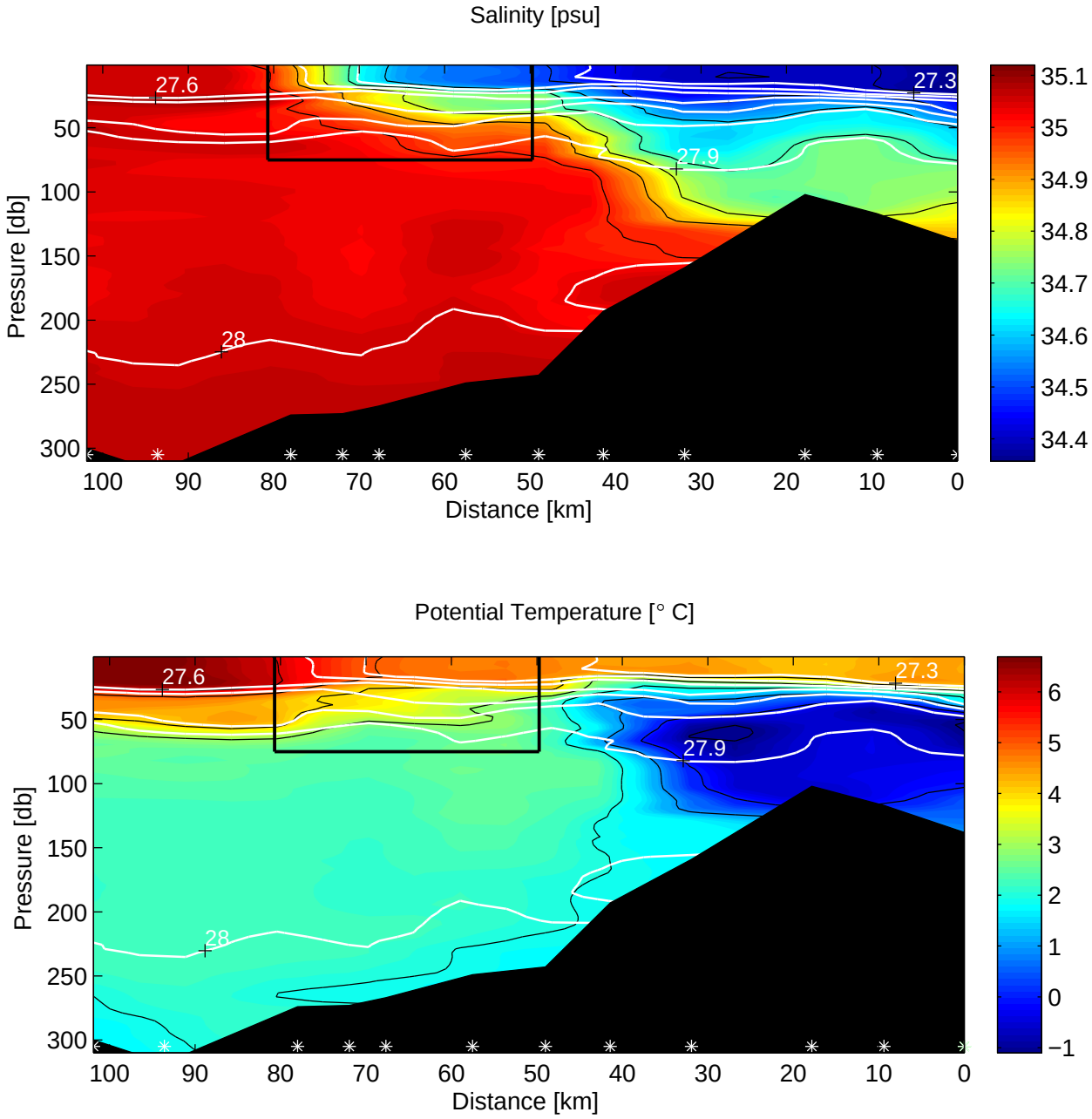

Figure 10: Salinity (*top*) and θ (*bottom*) based on 12 CTD stations at the southwestern flank of the Great Bank. The positions of the CTD stations are marked by the white asterisks at the bottom. The white contours show isopycnals with an equidistance of 0.1 kg m^{-3} in density. Isohalines and isotherms with equidistances of 0.1 psu and 1°C, respectively, are marked in black. The rectangle in the top 75 m indicates the HRSV. The Atlantic side of the front (southwest) is to the left, while the Arctic side (northeast) is to the right.

the results from the SST satellite data, which show that the strongest SST gradient occurred near the 6°C isotherm (Figure 9). In contrast to the salinity field, however, the temperature gradient was stronger at depth. At 75 m, the horizontal temperature gradient was about 3°C across 15 km (2.5°C on the Atlantic side and -0.5° on the Arctic side), resulting in a horizontal temperature gradient of approximately 0.2°C km^{-1} in the deep expression of the front. Over a distance of only 2 km, the strongest temperature gradient was observed at about 25 m depth, between the 2 and 3°C isotherms, resulting in a temperature gradient of approximately 0.5°C km^{-1} (Figure 10, bottom).

In general, significant thermohaline compensation was present, leading to nearly horizontal isopycnals across the front. Nevertheless, near the surface, densities on the Atlantic side ($\approx$ 27.6 σ_θ) were slightly higher than on the Arctic side ($\approx$ 27.3 σ_θ) due to shoaling of isopycnals in the frontal zone. This amounted to a density gradient of roughly 0.006 kg m^{-3} km^{-1} across the surface front, which was important for the frontal circulation (see below). In the deep expression of the front, no horizontal density gradients were detected. The pycnocline was centered around 30 m depth on both sides of the front, but it was stronger on the Arctic side of the front compared to the Atlantic side. On the Arctic side, the pycnocline occurred between the 27.3 and 27.8 σ_θ isopycnals over a depth range of about 25 m, while it extended over a depth of about 35 m between the 27.6 and 27.9 σ_θ isopycnals on the Atlantic side (Figure 10).

A lens of cold and fresh ArW with temperatures and salinities below 0°C and 34.8 psu was present on top of the Great Bank on the Arctic side of the front. AW with temperatures and salinities above 3°C and 35 psu, respectively, was found in the top 60 meters on the Atlantic side (Figure 10). Below 60 m, the temperature dropped to about 2°C on the Atlantic side of the front, and a cold layer with temperatures below 2°C was observed along the slope of the Great Bank (Figure 10, bottom).

Hydrography across the surface expression of the Polar Front

The high-resolution survey across the surface expression of the front revealed a patchy hydrographic structure in the frontal zone and oscillating isopycnals, which the CTD stations could not resolve (Figure 11). In section 22, two cold and relatively fresh cores of water were found around the northeastern end of the HRSV, which were accompanied by doming isopycnals (Figure 11, bottom). This shows that the cores were denser than the ambient water due to their colder temperatures. A distinct, but less conspicuous, water parcel with slightly lower salinity and temperature than its surroundings and a relatively high density, was found at a depth of about 30 m on the Atlantic side of the surface front, at the southwestern border of the HRSV (Figure 11, top). This parcel was predominantly observed along section 20, although traces of it were also visible in section 22 (Figure 11, bottom).

Hydrography in the surface expression of the Polar Front

In the top 30 m of the HRSV, the transition from high salinity and temperature on the Atlantic side of the front to lower salinity and temperature on the Arctic

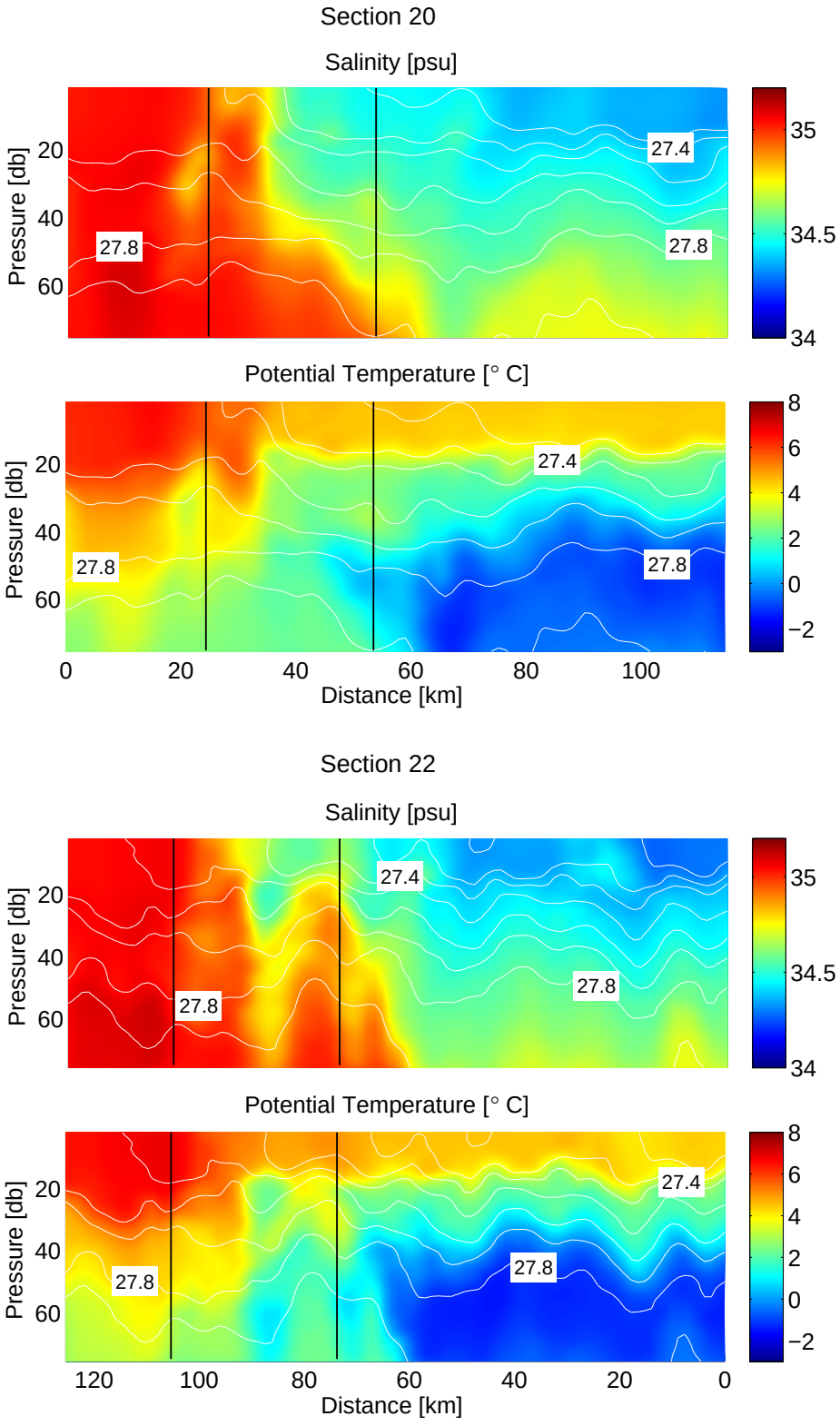

Figure 11: Salinity and θ for the cross-frontal sections 20 (*top*) and 22 (*bottom*). The HRSV is marked by two vertical black lines. The Atlantic side of the front (southwest) is to the left, while the Arctic side (northeast) is to the right. Isopycnals with an equidistance of 0.1 kg m^{-3} in density are shown as white lines.

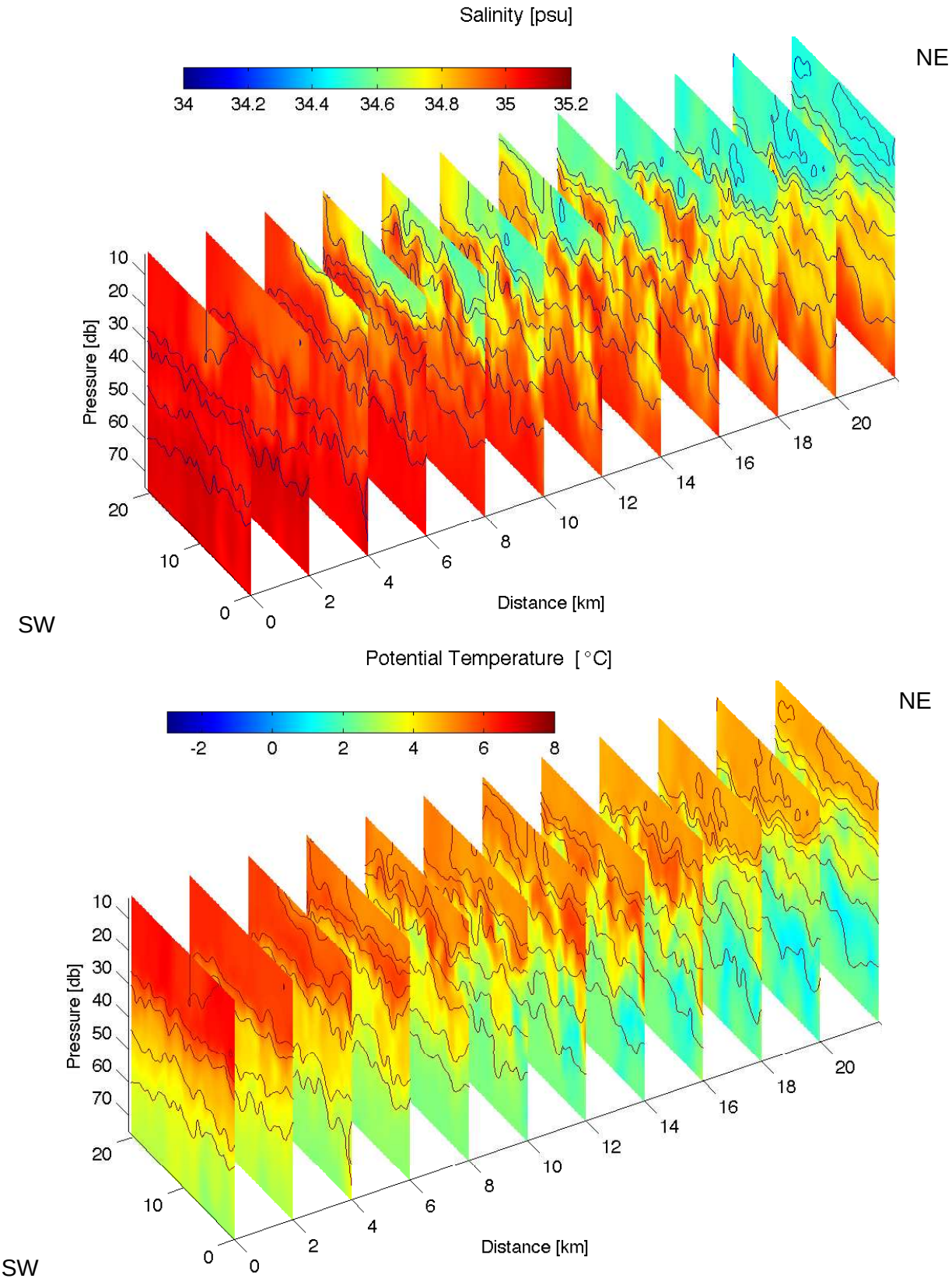

Figure 12: Salinity (*top*) and θ (*bottom*) in the short along-frontal sections. The Atlantic side of the front (southwest) is to the lower left, while the Arctic side (northeast) is to the upper right. Isopycnals with an equidistance of 0.1 kg m^{-3} in density are shown as dark lines.

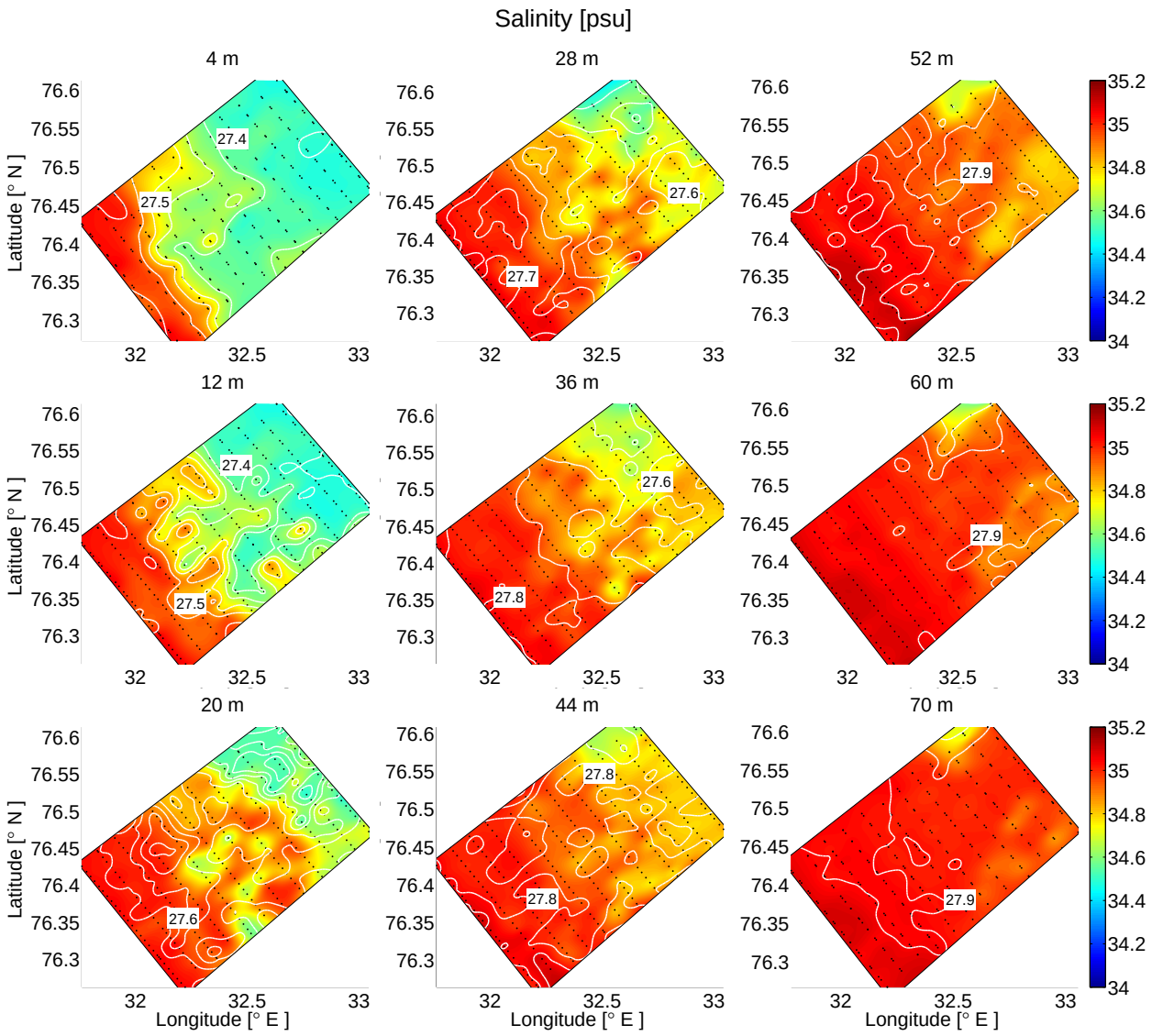

Figure 13: Salinity in the HRSV between 4 m (*top left*) and 70 m (*bottom right*). Isopycnals with an equidistance of 0.05 kg m^{-3} in density are shown as white lines. The data points from which the layers where interpolated are shown as black dots.

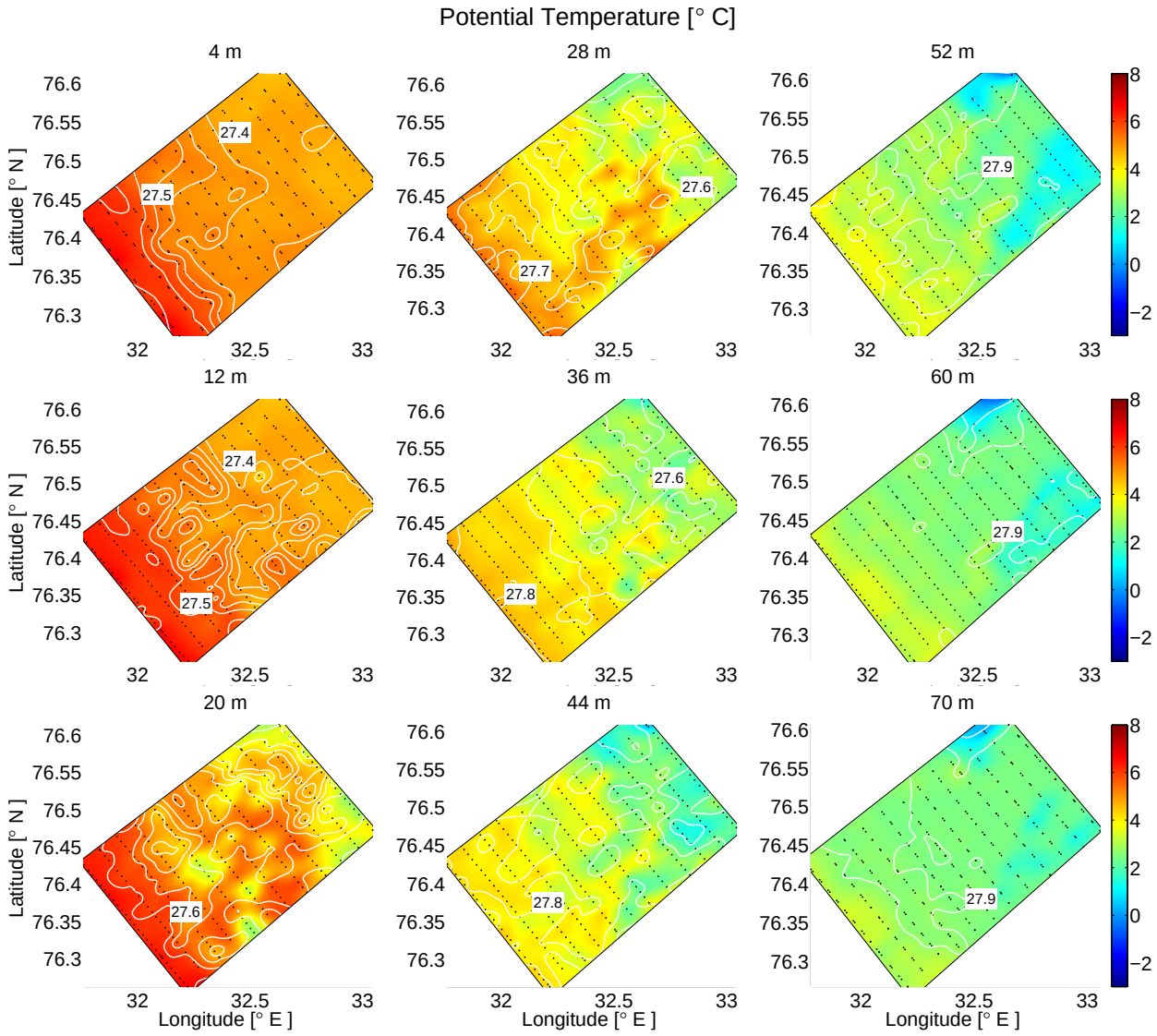

Figure 14: θ in the HRSV between 4 m (*top left*) and 70 m (*bottom right*). Isopycnals with an equidistance of 0.05 kg m^{-3} in density are shown as white lines. The data points from which the layers where interpolated are shown as black dots.

side marked the southwestern-most extent of the relatively fresh surface layer, where the surface expression of the BSPF was found (Figure 12). Within the surface expression of the front, the salinity gradient was strongest at the surface, from about 35 psu on the Atlantic to 34.5 psu on the Arctic side (Figure 12, top, and Figure 13). This is in contrast to the temperature distribution, which was relatively homogeneous in the upper 12 m across the entire HRSV, with a small temperature gradient from about 6°C southwest to 5°C northeast of the surface expression of the front (Figure 12, bottom, and Figure 14). A weak surface density gradient from 27.5 σ_θ on the Atlantic side to 27.3 σ_θ on the Arctic side of the front was present in the upper 10 meters (Figures 13 and 14). At 70 m, below the fresh surface layer, density was almost uniform in the entire HRSV, with a value around 27.8 σ_θ (Figures 13 and 14).

The hydrographic patchiness already observed in the long cross-frontal sections (Figure 11) was particularly conspicuous in the twelve short along-frontal sections that were concentrated along the surface expression of the front (HRSV). On the one hand, low density patches on the scale of 5-15 km were found at the surface on the Arctic side of the HRSV. This is clear from the enclosed isopycnals in the top 20 m (right sections in Figure 12). Also, a relatively fresh parcel of water with lower density was found in the top 20 m on the Atlantic end of the HRSV (left-most section in Figure 12). On the other hand, a water mass with higher salinities and densities than the ambient water was present in the top 20 m in middle part of the HRSV, causing the isopycnals to bend upward there (far side of central sections in Figure 12). The strongest salinity anomaly in the middle part of the HRSV was observed in the top 4 m (Figure 13, top left). Salinity controlled the density anomalies in these distinct water parcels in the top 20 m of the HRSV, since the temperature field was relatively homogenous in the surface layer. Moreover, the salinity distribution closely followed the density contours in the upper 12 m (Figure 13), providing further confirmation that salinity was most important for the formation of the density field near the surface.

In the northern-most corner of the HRSV, below the relatively fresh surface layer, water with low temperatures and salinities ($\approx$ 0-1°C and $\approx$ 34.7 psu, respectively) was found, where otherwise AW with higher salinities and temperatures was dominant (third column in Figures 13 and 14). This cold water mass was slightly denser than the ambient water, despite its lower salinity. This indicates that at depths below 50 m, temperature, rather than salinity, controlled the density.

On scales smaller than 5 km, hydrographic patchiness was observed in the middle part of the HRSV, between about 10 and 50 m depth (Figures 12, 13 and 14). This zone coincided with the location of the surface expression of the front. Accordingly, the isopycnals were very patchy there as well.

θS-profiles

θS-profiles from the interpolated sections (Figure 15) show that a significant amount of the water on the Atlantic side of the surface front was consistent with the AW definitions by Hopkins (1991) or Loeng (1991),

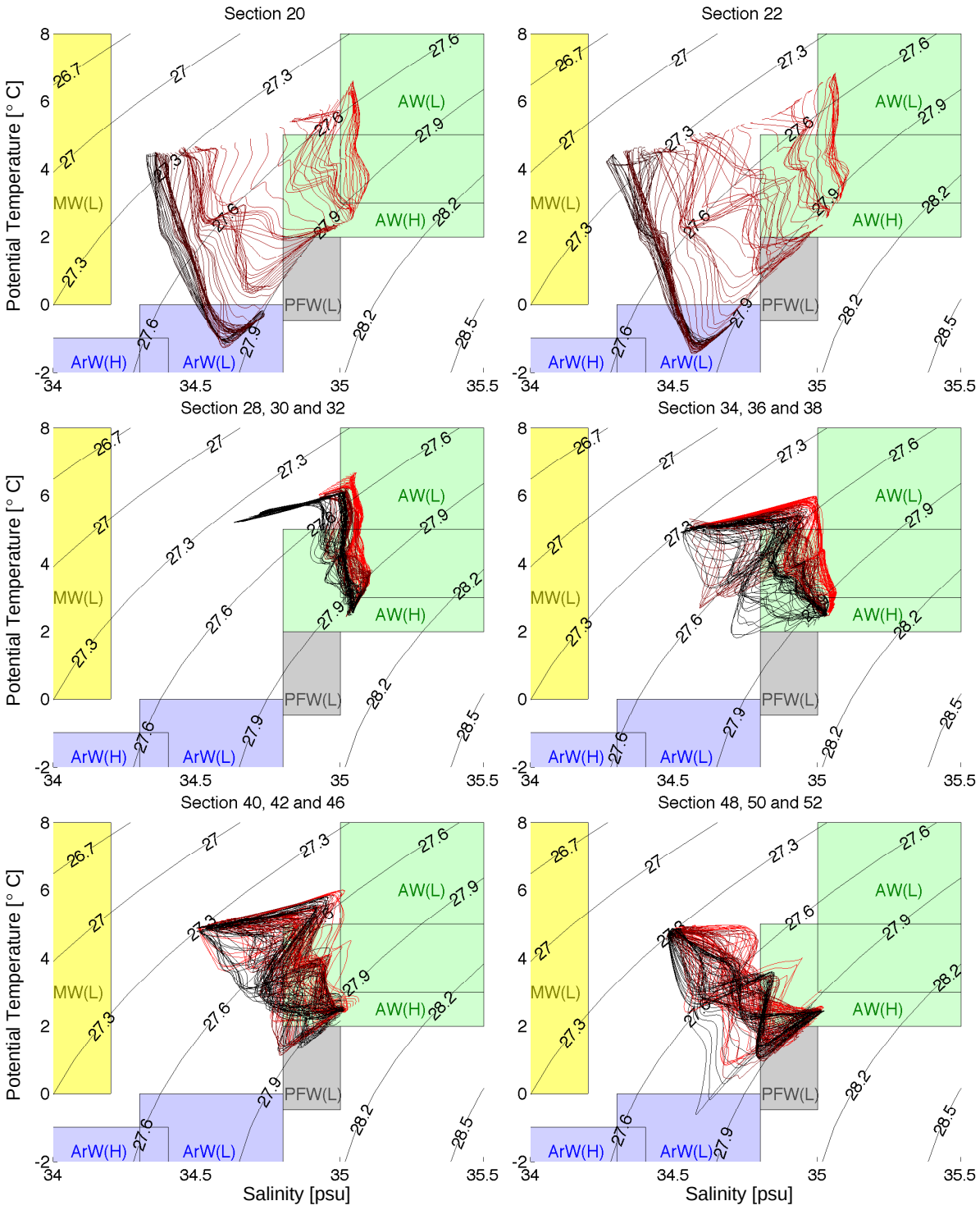

Figure 15: *Top row*: Uniformly spaced θS-profiles in the cross-frontal sections 20 (*left*) and 22 (*right*). Profiles on the Atlantic side of the front are marked in red, while the color shifts towards black on the Arctic side. *Middle and bottom row*: Uniformly spaced θS-profiles for the along-frontal sections. Three sections are shown in each subfigure. Profiles of the southwestern-most section (closest to the Atlantic side of the front) are shown in red, profiles from the central section in dark red, and profiles of the northeastern-most section (closest to the Arctic side of the front) are shown in black. Isopycnals with an equidistance of 0.3 kg m^{-3} are marked in black. Water masses according to Loeng (1991) and Hopkins (1991) are labeled with L and H, respectively (see Table 3).

Table 3: Temperature (T, °C) and salinity (S, psu) characteristics of water masses found near the BSPF based on Loeng (1991) and Hopkins (1991)

Water masses	Loeng		Hopkins	
Atlantic Water (AW)	T>3.0	S>35.0	2<T<5	S>34.8
Arctic Water (ArW)	T<0.0	34.3<S<34.8	-3<T<-1	S<34.4
Polar Front Water (PFW)	-0.5<T<2	34.8<S<35		
Melt Water (MW)	T>0.0	S<34.2		

which are summarized in Table 3. ArW, as defined by Loeng, was almost exclusively found in the deepest parts of the northeastern most profiles of section 20 and 22, which was not covered by the HRSV (Figure 15, top). Only the lowest parts of two profiles in the Arctic-most section of the HRSV had properties within the ArW definition (Figure 15, bottom right). These profiles were taken in the northernmost corner of the HRSV, where cold and fresh water was observed below 70 m (right columns in Figures 13 and 14). ArW, as defined by Hopkins, was not detected during the survey. Neither was meltwater (MW), originating from sea ice north of the BSPF. PFW was present in the deepest parts of the profiles near the northeastern end of the HRSV.

In the θS-profiles from the middle parts and the Arctic end of the HRSV, mixing lines were present that connected water mass properties from both sides of the front (near along-isopycnal lines leading to zigzag patterns in Figure 15). These mixing lines were accompanied by slight temperature and salinity inversions. On either side of the HRSV, the water column was more stably stratified, which was expressed in the more clear increase of density with depth. The θS-profiles on the Arctic side of the front spanned a wider range of density than the profiles on the Atlantic side, confirming that the stratification was strongest on the Arctic side of the BSPF.

Internal Rossby radius of deformation and horizontal density ratio

The latitude at the study site was about 76.5°N. Choosing the thickness of the relatively fresh surface layer to be $H = 50$ m, the density difference between that layer and the underlying AW to be $\Delta\rho = 0.4$ kg m^{-3}, and taking the mean density as $\rho_0 = 1027.8$ kg m^{-3} (Figure 10), the internal Rossby radius of deformation was approximately 3 km based on equation (3).

Based on Figure 11, estimates of the horizontal temperature and salinity gradients in the surface expression of the front were $\theta_x = 8 * 10^{-5}$ °C m^{-1} ($\approx$ 2°C over 25 km) and $S_x = 2 * 10^{-5}$ psu m^{-1} ($\approx$ 0.5 psu over 25 km). The thermal expansion coefficient α for 5°C and 34.9 psu at sea surface pressure is about $1.13 * 10^{-4}$ °C^{-1}, and the corresponding saline contraction coefficient β is $7.72 * 10^{-4}$ psu^{-1}. This gave a horizontal density ratio D_x of approximately 0.6 at the surface expression of the front based on equation (5).

3.3 Currents

The current field was predominantly barotropic, i.e. the flow direction and strength did not change signif-

icantly with depth.

During the survey of the HRSV, southwesterly winds dominated, with a mean strength of about 9 m s^{-1} (Figure 16). This wind field opposed the direction of the main currents.

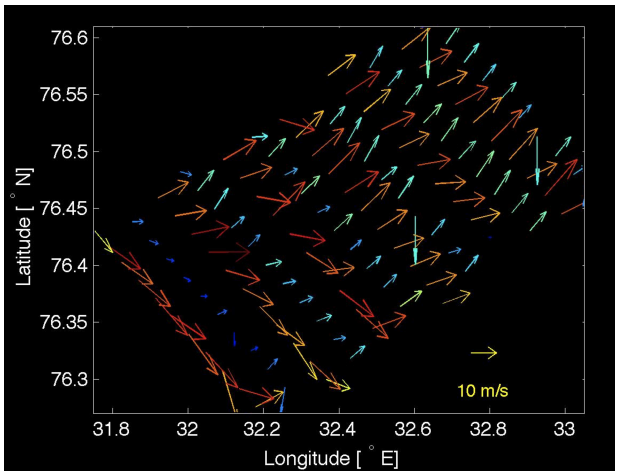

Figure 16: Wind at sea surface pressure during the HRSV sampling. The wind strength is indicated by the length and the color of the arrows. Note that there appears to have been a measurement bias with weaker wind recordings in every other section. This was not relevant for the present study and therefore not examined further.

Along-frontal velocity components

The dominant current feature was an along-frontal jet, which was located between the surface and the deep expression of the front and approximately confined between the 150 and 250 m isobaths on the southwestern flank of the Great Bank (Figure 17). Interestingly, two cores were present in the jet. The outer core was captured within the HRSV and located below the surface expression of the front, while the inner core was closer to the Great Bank, at the location of the deep expression of the front. According to the measured cross-track velocity components, the jet had a speed of about 20 cm s^{-1} at its cores in section 20 (Figure 17, top). In section 22, which was downstream of section 20, the cores were slightly further apart. Also, the outer core was weaker there ($\approx$ 15 cm s^{-1}), while the inner core closer to the Great Bank increased in width and speed to about 25 cm s^{-1}. This resulted in a measured velocity difference of approximately 10 cm s^{-1} between the two cores in section 22 (Figure 17, bottom).

The geostrophic and measured velocities in the upper 75 m of the jet were qualitatively similar, but the geostrophic velocities were significantly larger in magnitude, with a maximum speed between 40 and 50 cm s^{-1} at the cores (Figure 17, first and third subfigures). The weakening of the outer core and the strengthening of the inner core in section 22 was much more pronounced in the geostrophic currents than in the measured velocities (25 cm s^{-1} for the outer core versus 50 cm s^{-1} in the inner core, resulting in a velocity difference of about 25 cm s^{-1} in the geostrophic velocities).

Both the measured and the computed velocities surrounding the cores of the frontal jet were close to 0 cm s^{-1}, although some northwestward velocities between 10-20 cm s^{-1} on top of the Great Bank were present. This indicates the presence of a countercurrent on the Arctic side of the deep expression of front. Additionally, a weak countercurrent with velocities around 5 cm s^{-1} was measured between the cores of the along-frontal jet in section 22 (blue zone on top of the Great Bank and between the cores in section 22 in Figure 17). The computed geostrophic velocities of the countercurrents quantitatively matched the mea-

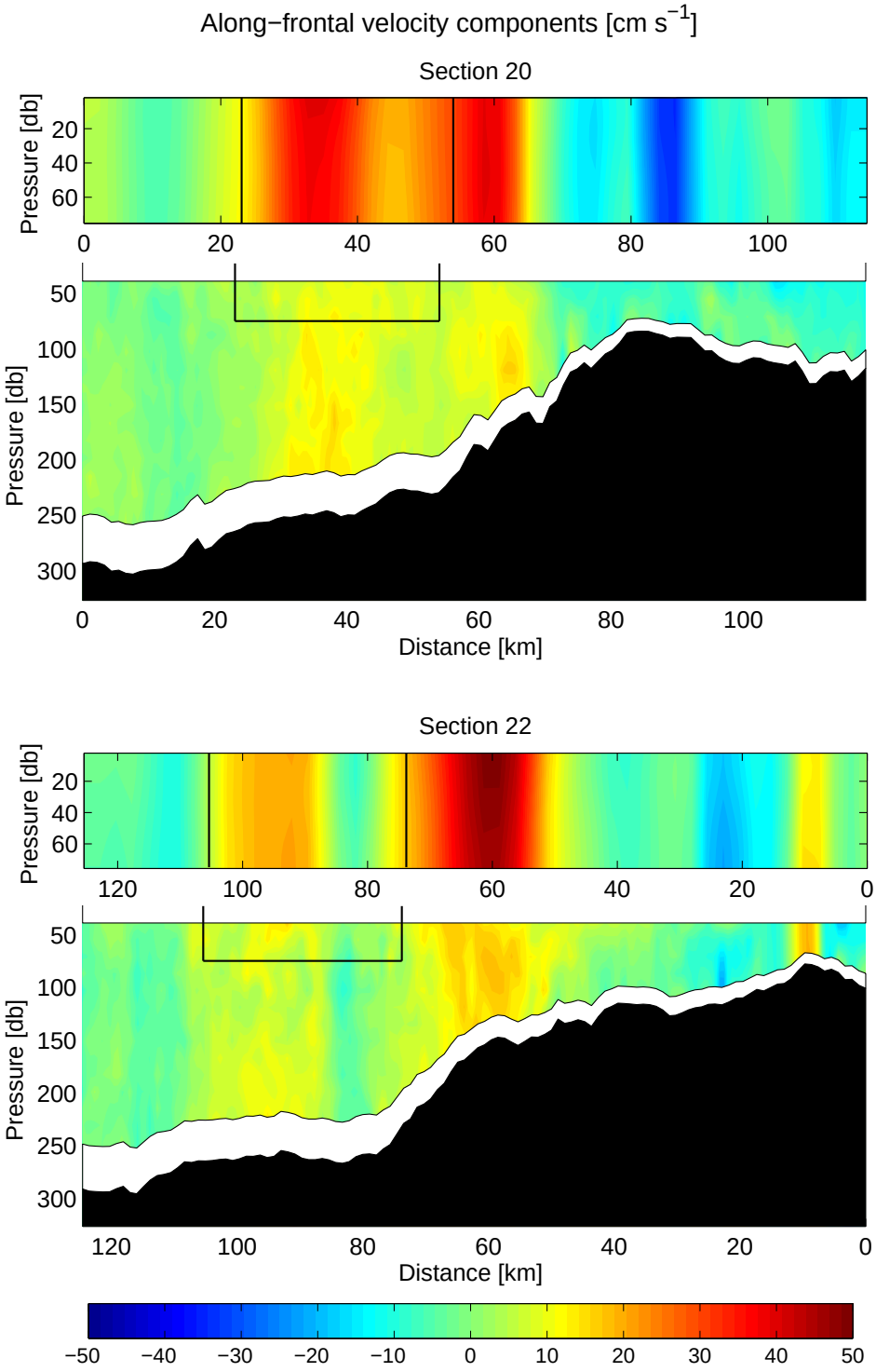

Figure 17: Measured ADCP (large subfigures) and calculated geostrophic (relative to 70 db, small subfigures) cross-sectional velocity components [cm s^{-1}] in the two cross-frontal sections 20 (*top*) and 22 (*bottom*). The extent of the HRSV is marked by the black rectangles. The bathymetry is shown in black. The Atlantic side of the front (southwest) is to the left and the Arctic side (northeast) is to the right.

sured velocities between the two cores in section 22, but they were significantly stronger and wider on top of the Great Bank ($\approx$ 40 cm s^{-1} instead of $\approx$ 10 cm s^{-1}, Figure 17, top).

In the far northeast of section 22, on top of the Great Bank, a narrow southeastward current with a width of about 5 km and a velocity of roughly 20 cm s^{-1} was observed (Figure 17, bottom).

Cross-frontal velocity components

Current components crossing the along-frontal sections were observed in addition to the along-frontal jet, although they were generally weaker, with maximal velocities around $\pm$ 10 cm s^{-1} (Figure 18). The strongest cross-sectional components, crossing the front from the Atlantic to the Arctic side, were observed in the northwestern-most parts of the HRSV (blue areas in the two right most sections at the bottom of Figure 18). The strongest Arctic-to-Atlantic-side components were detected in the sections southwest and northeast of the HRSV center (yellow areas at the bottom of Figure 18). Sections on the Atlantic-most side of the HRSV, as well as sections in the middle of the HRSV, had nearly zero cross-sectional velocity (green areas at the bottom of Figure 18). As for the along-frontal jet, the computed geostrophic cross-sectional components in the top 75 m qualitatively agreed with the measured ADCP cross-sectional currents, but they tended to be larger in magnitude. Maximal geostrophic velocity components across the short sections were on the order of 30 cm s^{-1} (Figure 18, top).

Measured horizontal currents

Strong southward velocities, with values close to 50 cm s^{-1}, were observed in the middle part of the HRSV (Figure 19, top and bottom). Relatively large currents in the opposite direction, i.e. towards the north, were measured northeast of the center of the HRSV. In the remaining sections of the HRSV, weaker currents on the order of 10 cm s^{-1} were found (Figure 19, top and bottom). In a given section, the direction of the current was fairly constant, while occasionally, it changed by more than 90 degrees between two neighboring sections (e.g. second and third sections from the left in Figure 19).

Tidal currents

Simulated tidal velocities at the time of the survey were between 0 and 10 cm s^{-1} (Figure 19, middle), and did not significantly influence the measured velocity field. This is evident from the negligible differences between the measured velocities before and after removal of the tides (top versus bottom of Figure 19). A noticeable influence of the tides was only found in a few sections. One of them was on the Arctic side of the HRSV, where the tides were counteracting the southwestward flowing currents, leading to bigger southwestward velocities after the tides were removed (northeastern most section in Figure 19).

Interpolated horizontal streamline currents

In general, the streamline-fitted, non-diverging flow varied little with depth, as expected from the predominantly barotropic nature of the flow (Figure 20).

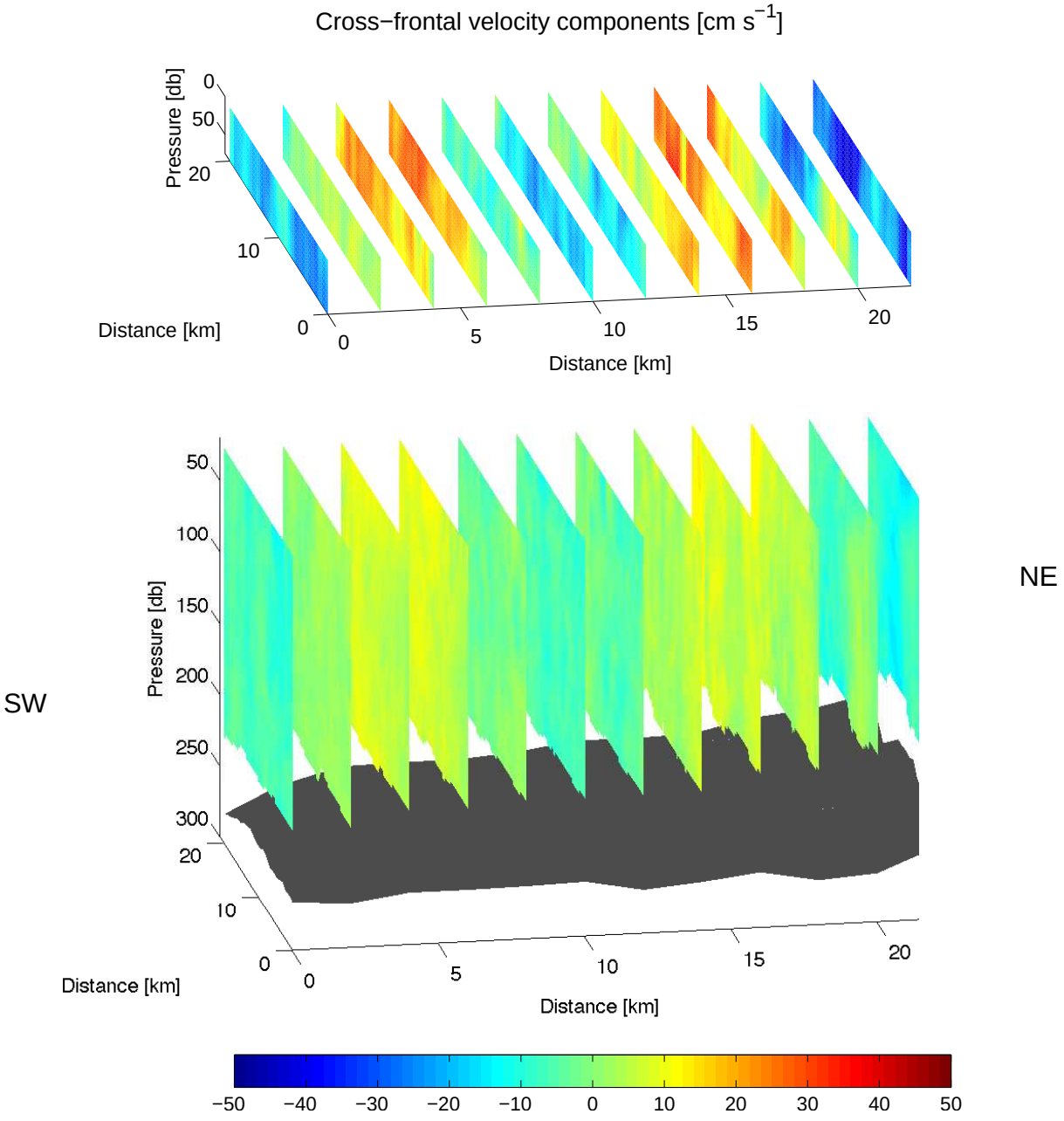

Figure 18: Calculated geostrophic (relative to 70 db, *top*) and measured ADCP (*bottom*) cross-sectional velocity components [cm s^{-1}] in the short along-frontal sections. The bathymetry is shown in black. Positive velocities are from the northeast (right) to southwest (left).

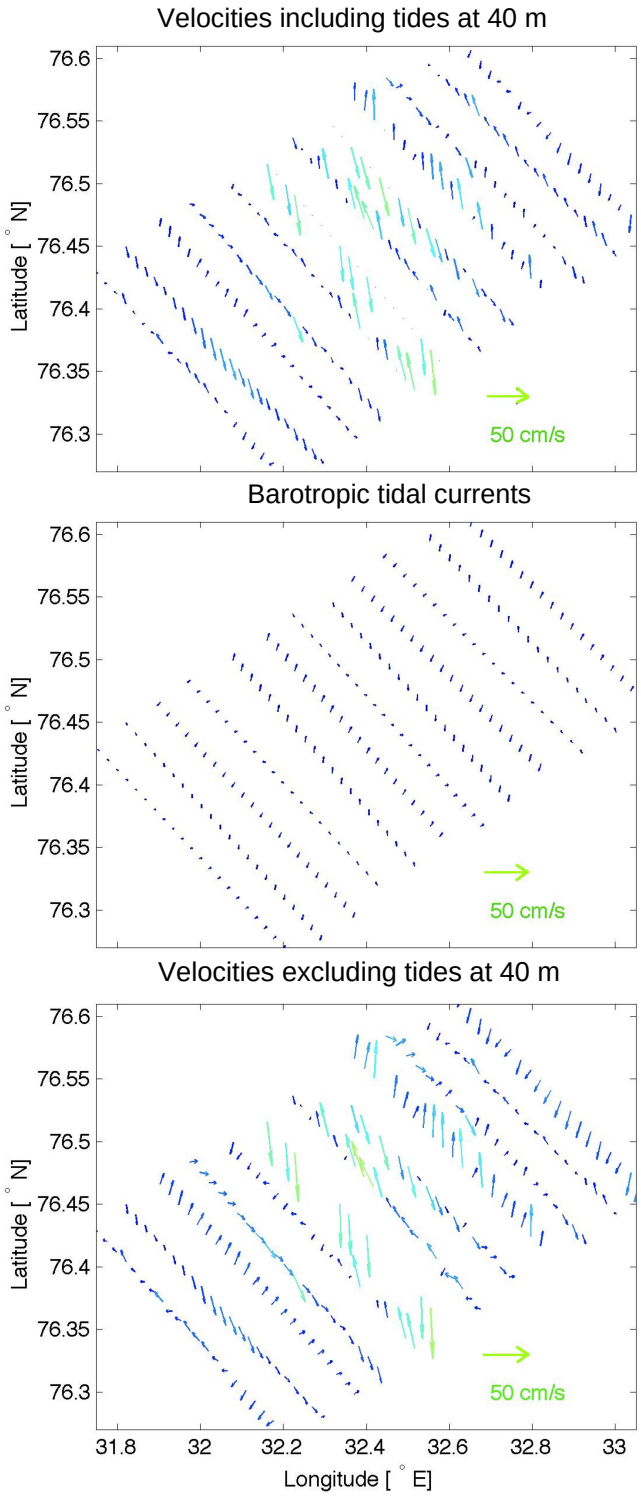

Figure 19: ADCP currents including tides (at ≈ 40 m, *top*), barotropic AOTIM5 tidal currents (*middle*), and residual currents after removal of tides (at ≈ 40 m, *bottom*). The speed of the currents is color coded and indicated by the length of the vectors.

The streamline flow revealed a major current in the middle of the HRSV towards the southeast, coinciding with the location of the measured outer core of the along-frontal jet (Figure 20). This current was perpendicular to the major salinity and temperature gradients in the surface expression of the front. At approximately 40 m, the southeastward flowing streamline current closely followed the border between high temperatures and salinities on the Atlantic side, and the low temperature and salinity on the Arctic side of HRSV. This is visible in the southward bending of the current and a consecutive northward flow around a parcel of low temperature and salinity (Figure 20, top). At a depth near 72 m, the streamline function revealed a meandering current in the middle of the HRSV, while a circular flow emerged at about 140 m (Figure 20, middle and bottom left, respectively).

On the Arctic side of the HRSV, the streamline current flowed parallel to the front in the opposite direction of the main along-frontal jet (Figures 20). This countercurrent matched the location of the measured countercurrent between the two cores of the along-frontal jet in section 22 (Figure 17). Changes in the direction of the streamline flow took place in the zones where the measured cross-sectional components shifted direction (compare Figure 20 with cross-sectional components in Figure 18).

Occasionally, the the streamline current strongly opposed the underlying current data. This is in particular visible in the northeastern-most section (compare Figure 19 with Figure 20).

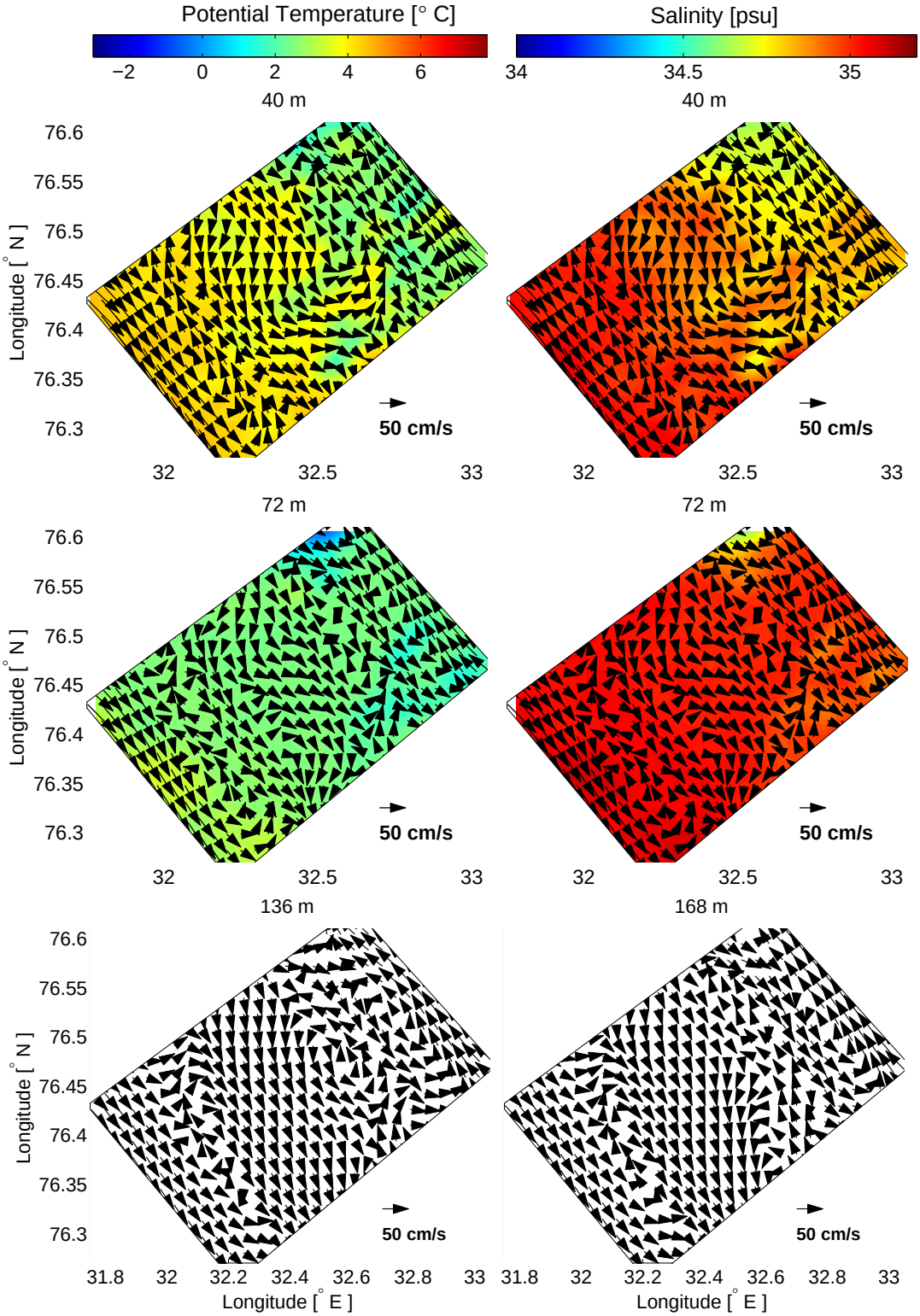

Figure 20: Streamline currents within the HRSV at 40 m (bin 2) and 72 m (bin 4) with θ and salinity in the background (*top two left* and *right*, respectively), and streamline currents at 136 m (bin 8, *bottom left*) and 168 m (bin 10, *bottom right*).

3.4 Biology

Plankton distribution across the surface expression of the Polar Front

A conspicuous surface fluorescence maximum was present in the top 20 m on the Atlantic side of the surface front. For the most part, this maximum was outside the HRSV. Weaker subsurface fluorescence maxima were found northeast of the HRSV between about 20 and 40 m depths (Figure 21, first and third subfigure). These subsurface maxima were located at the bottom of the low salinity surface layer, near the pycnocline, between the 27.5 and 27.7 σ_θ isopycnals. Fluorescence in the rest of the study area was very low.

Zooplankton was not observed in the area of the strong fluorescence maximum on the Atlantic side of the surface front, and the northeastern-most observed areas of high zooplankton abundance were closer to the HRSV, i.e. the surface frontal zone, than it was in the case of fluorescence (Figure 21, second and fourth subfigure). Maximum zooplankton abundances of 300 to $400 * 10^3$ individuals m^{-3} were detected in the upper 20 m in the central parts of sections 20 and 22, where fluorescence was nearly absent. In section 20, two isolated areas of high zooplankton abundance were present. One was located in the middle of the HRSV, while the other was on the Arctic side of the HRSV (Figure 21, second subfigure). These areas of maximum zooplankton abundance coincided with the location of the two cores of the along-frontal jet (Figure 17, top). In section 22, several smaller patches of zooplankton were observed near the Arctic end of the HRSV (Figure 21, fourth subfigure). The location of these patches coincided with the weak countercurrent between the two cores of the along-frontal jet and the cold and fresh cores of water, which were accompanied by doming isopycnals.

Plankton distribution in the surface expression of the Polar Front

In the HRSV, fluorescence was highest (≈ 1.5) and most widespread on the southwestern end in the top 20 m (Figure 22, top). This area of high fluorescence was part of the fluorescence maximum observed on the Atlantic side of the surface front (Figure 21). Fluorescence maxima decreased in intensity to about 0.75 and increased in depth to about 20-50 m towards the Arctic side of the HRSV (Figures 22, top, and Figure 23). Also, the fluorescence distribution became increasingly patchy in the northeast direction. In a similar fashion, zooplankton shifted from a presence in the top 20 m on the Atlantic side of the HRSV to subsurface depths towards the northeast, where they became more patchy (Figure 22, bottom, and Figure 24). Zooplankton was most widespread between 10 and 20 m depths, where also the highest abundances were observed, reaching up to $500 * 10^3$ individuals m^{-3} (Figure 24). The deepest zooplankton patches in the HRSV were found at a depth of about 50 m on the Arctic side, with values around $250 * 10^3$ individuals m^{-3}. These deep zooplankton patches coincided with water mass parcels that were cold relative to their surroundings (compare bottom right of Figures 12 and 22).

Patchiness was a conspicuous feature in both the fluorescence and zooplankton distribution, although

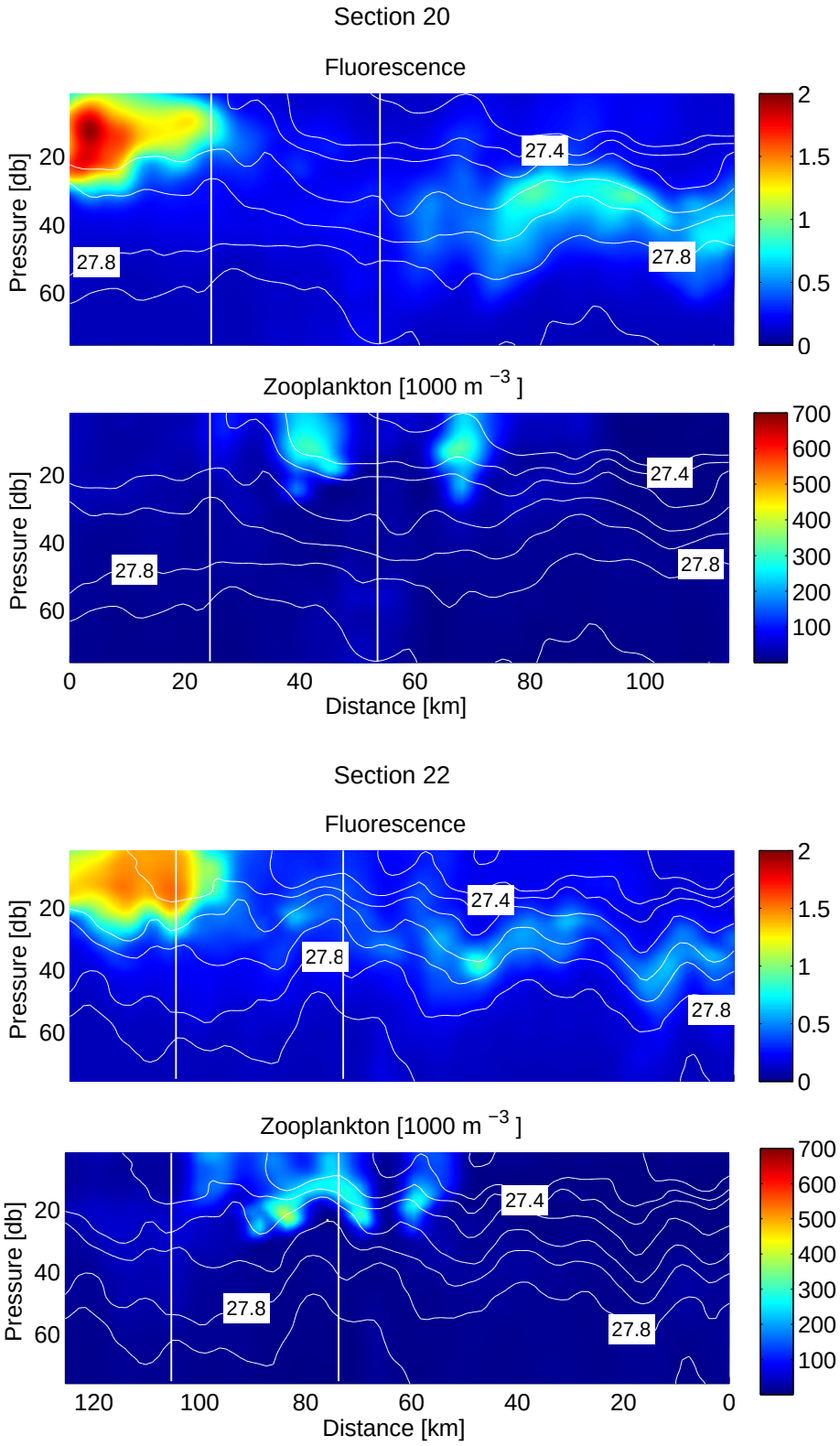

Figure 21: Fluorescence and zooplankton ($>$ 250 μm ESD) in the two cross-frontal sections 20 (*top*) and 22 (*bottom*). Isopycnals with an equidistance of 0.1 kg m^{-3} in density are shown as white lines. The extent of the HRSV is marked with two vertical white lines. The Atlantic side of the front (southwest) is to the left, while the Arctic side (northeast) is to the right.

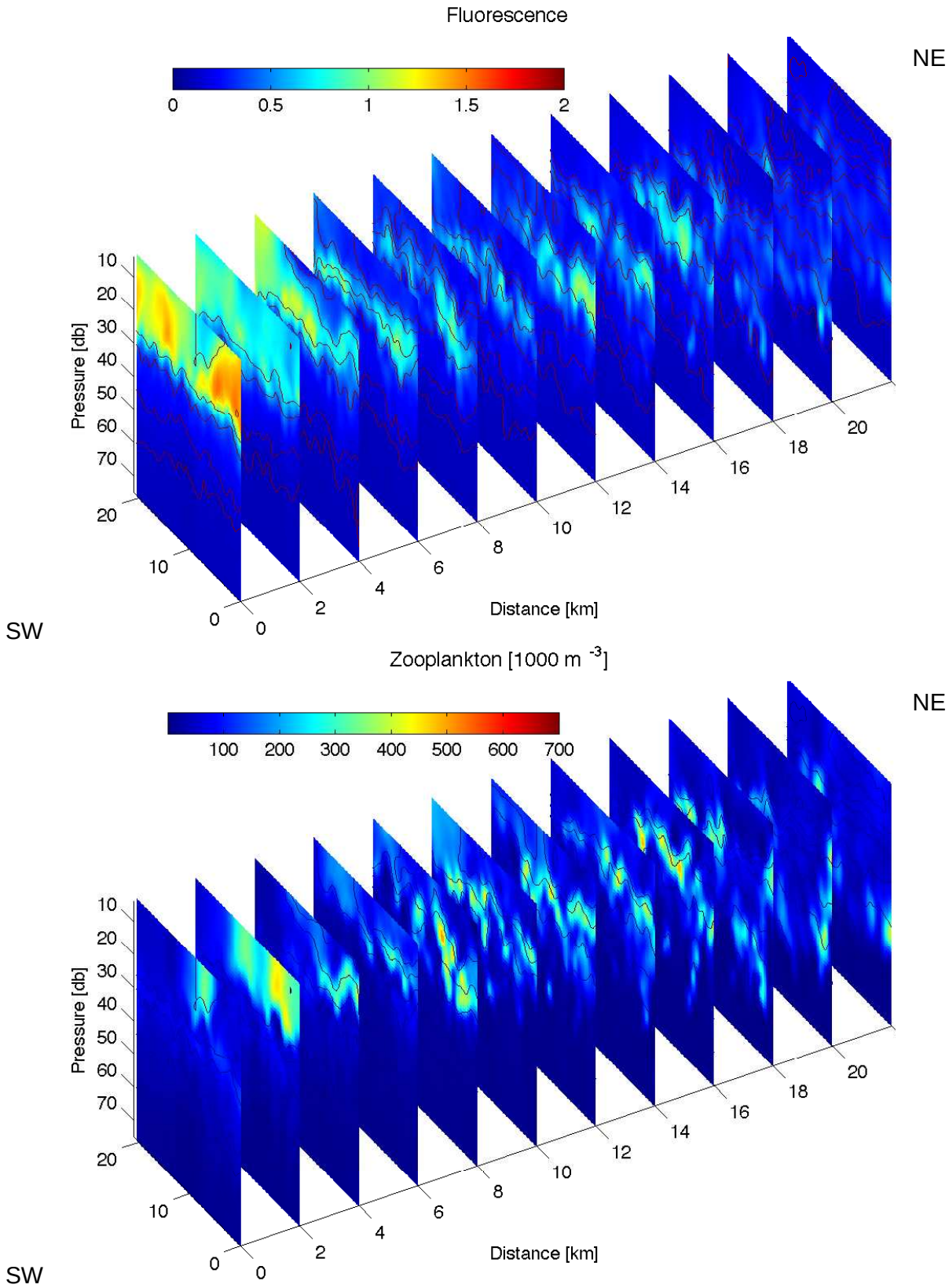

Figure 22: Fluorescence (*top*) and zooplankton (> 250 μm ESD, *bottom*) in the short along-frontal sections. Isopycnals with an equidistance of 0.1 kg m^{-3} in density are shown as dark lines. The Atlantic side of the front (southwest) is to the lower left, while the Arctic side (northeast) is to the upper right.

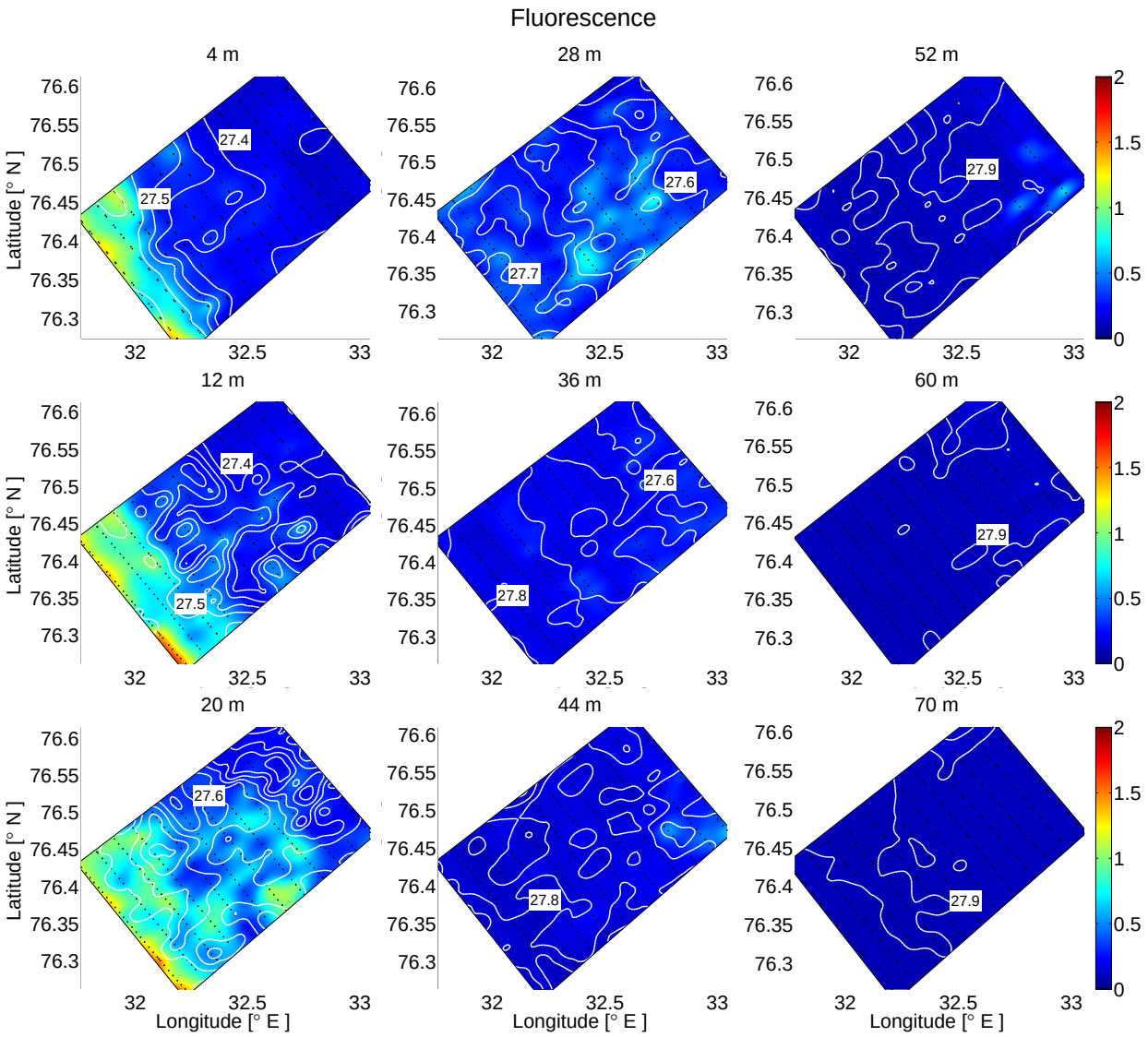

Figure 23: Fluorescence in the HRSV between 4 m (*top left*) and 70 m (*bottom right*). Isopycnals with an equidistance of 0.05 kg m^{-3} in density are shown as white lines. The black dots indicate the data points from which the depth layers were interpolated.

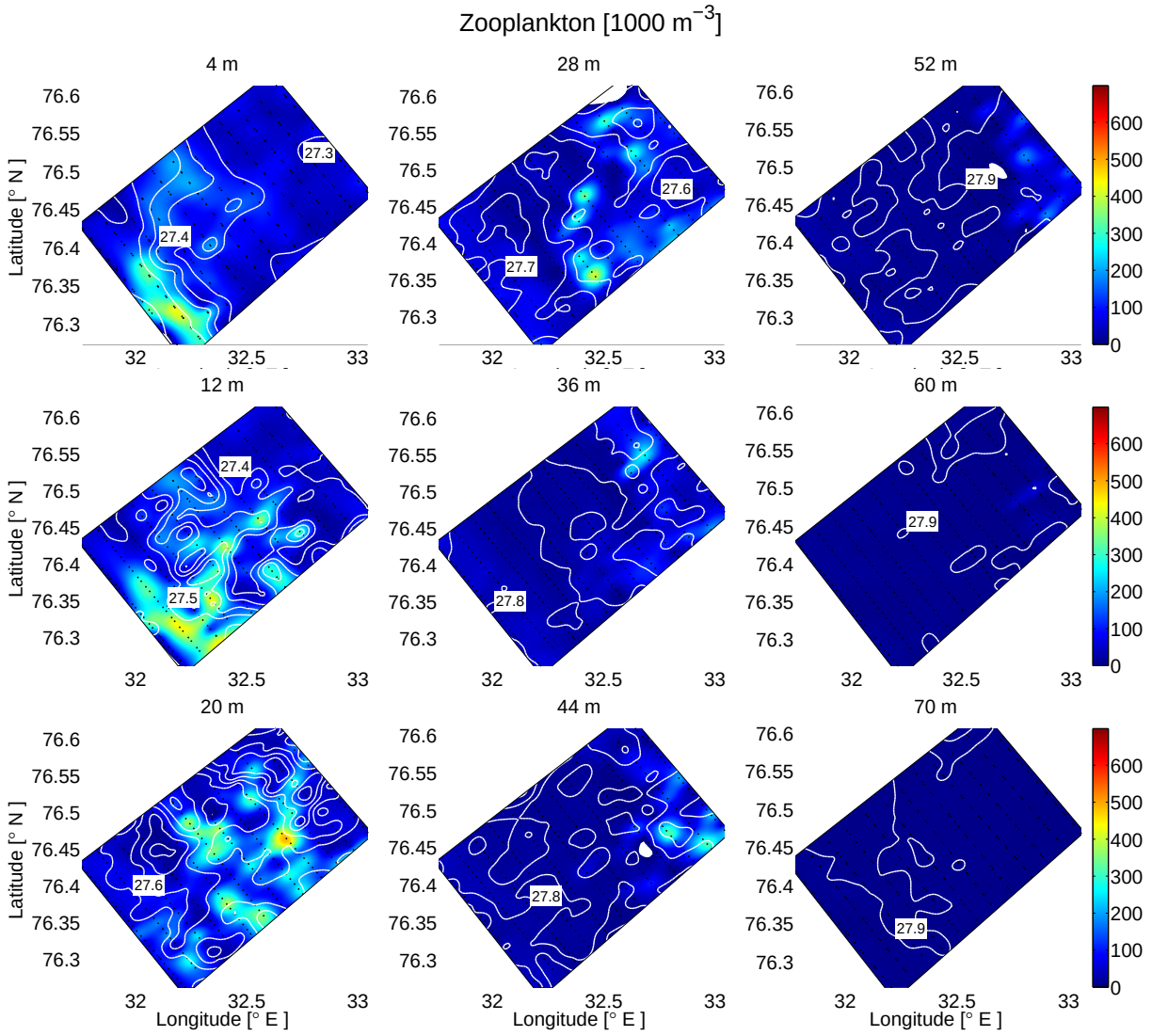

Figure 24: Zooplankton (> 250 μm ESD) in the HRSV between 4 m (*top left*) and 70 m (*bottom right*). Isopycnals with an equidistance of 0.05 kg m^{-3} in density are shown as white lines. The black dots indicate the data points from which the depth layers were interpolated. Note that white areas occurred due to interpolation below zero and should be regarded as zero zooplankton abundance.

it tended to be more pronounced on the small scale for zooplankton (Figure 22). The horizontal scale of the patches was on the order of 2-5 kilometers, consistent with the hydrographic small-scale variability (Figures 23 and 24). Interestingly, the phyto- and zooplankton patches in the upper 20 m often coincided with AW patches, while between 20 and 50 m, the smaller fluorescence maxima and zooplankton abundances were located in water parcels with low salinities and temperatures (compare Figures 13 and 14 with Figures 23 and 24). The fluorescence and zooplankton patches were generally confined between isopycnals, while the constraint was strongest in the upper 10-20 m (Figures 23 and 24).

In isolated areas on the Atlantic side of the HRSV, fluorescence was relatively low, while zooplankton abundances peaked there (left in Figures 22, 23 and 24). These areas were also less saline than the surroundings (compare top left of Figure 12 and left of Figure 22). For example, in the relatively fresh water parcel that was found in the top 20 m of section 28, a significant fluorescence minimum was present (≈ 0.75 instead of 1 to 1.5), while zooplankton abundances peaked with approximately 400 instead of $50 * 10^3$ individuals m^{-3} compared to the rest of section 28 (left most section in Figure 12). Also, in the sections immediately adjacent to section 28, fluorescence was concentrated on the northwestern parts, while zooplankton abundances were highest in the southeastern parts of the sections (second and third section from left in Figure 22). As the plankton patches increased with depth and were found further to the northeast, the fluorescence and zooplankton distributions became more congruent (Figures 22, 23 and 24).

4 Discussion

Compared to previous surveys on the BSPF, the strength of the presented data set lies in its high resolution, its near synopticity and the combination of physical and biological observations.

4.1 Data and methods

Quality of the ADCP data

The variance of the raw along-track velocity components was much higher compared to the cross-track velocities, and might be biased (Figures 7 and 8). Perhaps the variance of the ship speed increased the variance in the along-track components, although high variance in the along-track components remained after removing the ship speed from the raw data. The pitch and roll of the ship may have contributed to the high variance of the velocity components, as corrections for these motions were not possible due to a lack of information. On the other hand, using 5-minute averages probably smoothened the effects of the pitch and the roll. The source of the high variance in the along-track components remains uncertain, but data filtering removed most of the high variance.

In additon to the high variance in the along-track raw data, the fact that only one of the four beams had %-good values close to 100 was initially not promising. In other studies, only pings with 100% good values are used (e.g. Nardelli *et al.*, 2001). If the same restrictions would have been applied to this survey, an insufficient amount of data would have remained

for the analysis. It was therefore assumed that the threshold used to classify a ping as good or bad was set too high, legitimizing the use of the low %-good values. This premise appears reasonable when keeping in mind that the error velocities and echo amplitudes of the time-averaged raw data were within acceptable ranges. Also, the computation of geostrophic velocities from the hydrographic data resulted in current fields that closely resembled the pattern of the measured cross-sectional currents, demonstrating that the measured currents were in fair agreement with the hydrography. Nevertheless, some uncertainty about the quality of the ADCP data and in particular the along-track components remains. Hence, the horizontal velocity fields based on both the along- and the cross-track velocities and the fitted streamline flow are highly uncertain.

ADCP processing

The conventional processing method, which entails grouping the beams based on their temporal relation, was used to construct velocity profiles (Trump & Marmorino, 2002). It is questionable if this was optimal for the dynamical flow in this study. When the measured current features are fine-scaled and turbulent enough, the spreading of the four beam becomes larger than the horizontal length scale of the current features at depth. Consequently, different velocities are measured by the four beams. This may have been the case in the present survey. An alternative method, where beams are grouped based on their spatial relation, may therefore have been preferable (Trump & Marmorino, 2002). However, due to time constraints, this method was not attempted here.

Interpolation

Interpolation methods require statistical assumptions about the underlying distribution, and postulate a certain degree of smoothness of the data field to be displayed (Emery & Thomson, 2004). For the vertical sections, the choice of the interpolation function was not very critical, as the sections contained a relatively dense grid of measured data points. Consequently, different interpolation functions did not produce very different results (not shown). The particular choice of the interpolation method for the horizontal fields was more critical, because the measured data points were farther separated from each other. For the hydrographic and planktonic data, an interpolation routine was chosen that is capable of interpolating scattered data sets even if there are replicates (D'Ericco, 2006). Furthermore, the chosen routine extrapolates smoothly into convex hulls of data, which minimized unrealistic edge effects.

For the horizontal current fields, objective analysis (OA) was chosen since it results in optimal interpolation in the least squares sense (Emery & Thomson, 2004). However, meeting the stationary and homogeneity assumptions of OA was not fully possible in the dynamical frontal zone. Also, Bretherton *et al.* (1976) stressed that good estimates of the statistics of the field are important for a reliable OA. Here, the statistics used were the decorrelation scales in the eastward and northward directions and the covariance function, which were all challenging to estimate. Even though the internal Rossby radius of deforma-

tion, which is closely related to the decorrelation scale across the front, was estimated to be about 3 km, the eastward and northward decorrelation scales needed to be longer in order to obtain realistic results (not shown). The reason was likely that the coordinate system used in the OA was not adjusted to the orientation of the front, which implies that the eastern and northern decorrelation scales used in the OA did not align with the along- and cross-frontal axes. Instead, the axes of the eastern and northern decorrelation scales crossed the front diagonally. As the decorrelation scale across a front is much shorter than along the front, the decorrelation scales crossing the front diagonally should be larger than the internal Rossby radius of deformation. The final values for the eastern and northern decorrelation scales (15 km) were subjectively determined based on the realism of the OA solutions. This underlines the fact that the choices of the statistical values employed by the OA is not very objective (Emery & Thomson, 2004). Despite the somewhat subjective choice of the decorrelation scales, the streamline interpolation resulted in a flow field that reflected the measured flow field and the computed geostrophic currents. The high-resolution of the data set, which is known to improve the accuracy of the OA, is a likely reason for the generally good match (Bretherton *et al.* , 1976).

Along- versus cross-frontal sampling

Along-frontal sampling is recommended by Rixen *et al.* (2003a) for hydrographic and bio-chemical variables in sufficiently developed fronts where frontal waves occur. In such cases, sampling in the across-front direction has an increased and undesired Doppler effect, which results from the movement of the ship in the direction of the frontal waves. To avoid this bias, the high-resolution sampling in this study took place in the along-frontal direction in this study (Figure 1), which may in part explain the high quality of the hydrographic and biological data. However, a cross-frontal strategy may be superior for the ADCP survey. Fong & Monismith (2004) evaluated several different RD broadband ADCP instruments (such as the one used in this study), and found that there was an error in the along-track velocities, which was biased towards the direction in which the ship was traveling. The high variance in the along-track components in this study may to some extent be explained by the same type of bias. The cross-track velocities are not affected by the ship's direction of motion, which is in agreement with the increased quality of the cross-track velocities.

If the high-resolution sampling strategy would have been cross-frontal instead of along-frontal, the major along-frontal current would have been captured by the less biased cross-track velocities. This would have increased the confidence that the dominant flow was measured accurately. As a trade-off, such a sampling strategy might have required discarding velocities measured in the along-track direction, as the along-track bias could have been on the same order of magnitude as the weaker cross-frontal components (Fong & Monismith, 2004). Hence, it is difficult to determine which sampling strategy would have been optimal when considering the advantages and disadvantages for hydrographic, biological and direct velocity

data, without having a comparison from an equivalent cross-frontal data set.

High-resolution versus large and long-term surveys

Finally, when measuring a dynamical system such as the BSPF, collecting a sufficient amount of data in space and time is crucial in order to capture both the short- and the long-term variability of the system. High-resolution and long-term data sets are, however, expensive to obtain. In this study, high-resolution sampling with a small spatial and temporal coverage was prioritized to resolve the sub-mesoscale features of the front. This nearly synoptic sampling program minimized the interpretation problems that can occur when sampling is done from a slow-moving ship in frontal zones with large velocity shear and advection (Johannessen *et al.* , 1977). Moreover, it permitted a novel description of small-scale variability in the front that has not been made before, which is the main strength of this data set. The unavoidable compromise of this quasi-synoptic sampling strategy is that long-term and large-scale behaviors of the front are unknown. In particular, phenomena such as meanders and large eddies in the BSPF with horizontal scales of approximately 30-50 km, cannot be discussed in this study (Berezutskii *et al.* , 1994).

4.2 Physical properties of the BSPF

Hydrographic gradients across the Polar Front

The ratio of the horizontal temperature and salinity gradients (D_x) in the surface expression of the BSPF was smaller than one, indicating that the importance of the horizontal temperature gradient was smaller in terms of density than in the case of the salinity gradient. Near the surface, salinity was therefore dominant in the formation of the across-frontal density gradient, which ultimately led to the along-frontal current discussed below. The same situation has been observed previously in the BSPF and the Arctic Ocean Front (Parsons *et al.* , 1996; May & Kelley, 2002). Solar heating of the surface layer, which can effectively transport heat down to a depth of 50-60 m in the Barents Sea during the course of the summer (Ingvaldsen & Loeng, 2009), was probably responsible for the weak horizontal temperature gradient near the surface.

Thermohaline compensation observed below the mixed layer appears to be a ubiquitous feature of the BSPF (Berezutskii *et al.* , 1994; Gawarkiewicz & Plueddemann, 1995; Parsons *et al.* , 1996). This is an important precondition for isopycnal mixing of AW and ArW, which leads to the formation of PFW.

The horizontal salinity and temperature gradients in the surface and the deep expressions of the front were very similar to those observed by Parsons *et al.* (1996) on the southern flank of the Spitzbergen Bank (0.03 versus 0.06 psu km^{-1} near the surface and 0.02 psu km^{-1} at depth for the salinity gradients, and 0.07 versus 0.11°C km^{-1} near the surface and 0.20 versus 0.22°C km^{-1} at depth for the temperature gradients).

The salinity gradient in this study suggests that the 34.8 psu isohaline can be used as an identification mark for the location of the surface BSPF near the Great Bank, which is similar to the suggested 34.6 psu isohaline on the southern flank of the Spitzbergen Bank (Parsons *et al.* , 1996). The strongest tempera-

ture gradient serving as a frontal identification tag was observed between the 2 and 3°C isotherms at 25 m, which is slightly cooler and shallower than suggested by Johanessen & Foster (1978), but agrees with Parsons *et al.* (1996).

It should be added that the calculation of the salinity and temperature gradients was to some extent subjective, as it depended on the choice of depth and distance over which the gradients were computed. Depths that were representative for the surface and deep expressions of the front, and distances over which the changes in salinity and temperature were most pronounced, were selected.

Barotropic flow

Both measured and computed currents revealed a largely barotropic flow in the BSPF, which at first seemed in accordance with the general barotropic flow in the Barents Sea (Loeng, 1991; Slagstad & McClimans, 2005). However, Loeng specifically mentioned an exception in the area west and south of the Great Bank, where AW sinks below the lighter ArW. In this region, the direction of the current in the deep layer was found to oppose the surface direction. Such opposing currents were not observed in this study. Instead, barotropic forcing appears to have determined the flow, which was also suggested for the barotropic flow in the BSPF on the southeastern slope of the Spitzbergen Bank (Parsons *et al.* , 1996).

A barotropic recirculatory flow of AW has been observed and modeled on the southern flank of the Spitzbergen Bank below the 250 m isobath (Gawarkiewicz & Plueddemann, 1995; Parsons *et al.* , 1996). If this recirculatory AW enters far enough into the Hopen Deep, it would be visible as a northwestward barotropic AW flow on the southwestern flank of the Great Bank. However, in the present study, a southeastward along-frontal current was observed instead, indicating that the frontal circulation at the Great Bank was decoupled from the AW recirculation. Hence, it can be inferred that the recirculatory AW did not extend far into the Hopen Deep during this survey. This confirms findings by Skagseth (2008), which indicate that the recirculating AW follows a relatively short pathway into the Bear Island Trench before returning to the Norwegian Sea.

Topographic control of the BSPF

The more pronounced SST gradient near the BSPF in the western Barents Sea compared to the east of the Great Bank confirmed that the BSPF is more confined in the western Barents Sea than in the east, which is explained by stronger topographic control in the west (Johannessen & Foster, 1978; Gawarkiewicz & Plueddemann, 1995; Parsons *et al.* , 1996; Ellingsen *et al.* , 2008). Despite the potential influence of higher water temperatures and smaller amounts of sea ice due to global warming on the position of the BSPF, a model by Ellingsen *et al.* (2008) predicted that the location of the BSPF will remain stationary in the west over the next 50 years due to topographic control. The Central Bank, which lies directly south of the Great Bank, has been described as a transitional zone towards a more weakly topographically controlled front in the east (Ellingsen *et al.* , 2008). Topographic constraint is therefore expected at the Great Bank, al-

though it might be weak. From this study, it appears that topography was important for the position of the BSPF, as the front was nearly parallel to the isobaths on the southwestern flank of the Great Bank. Also, the front was confined between about the 125 and 275 m isobaths, which is in fair agreement with the isobath constraints of the BSFP on the southeastern slope of the Spitzbergen Bank (Johannessen & Foster, 1978; Harris *et al.* , 1998). However, the short distance of the BSPF front covered by this study does not permit a final evaluation of the importance of topographic steering near the Great Bank.

Structure of the geostrophic along-frontal jet

Due to its higher density near the surface, AW was submerged under the lighter ArW, presumably leading to the surface and deep expressions of the front on the southwestern flank of the Great Bank. Since the geostrophic along-frontal jet was southeastward, there must have been a pressure gradient from the Atlantic to the Arctic side of the front. To some extent, the pressure gradient can be explained by the higher densities of AW compared to ArW near the surface, leading to a pressure gradient from southwest to northeast. Additionally, the spreading of lighter ArW on top of AW may have caused an increased sea surface height (SSH) on the Atlantic side of the front, which would have supported the pressure gradient towards the Arctic side of the front (Figure 25).

There was a clear link between the two cores of the along-frontal jet and the surface and deep expressions of the front. The outer core can be interpreted as a geostrophic flow driven by the pressure gradient across the surface expression of front, which was at least partially driven by the cross-frontal density gradient (left orange circle in Figure 25).

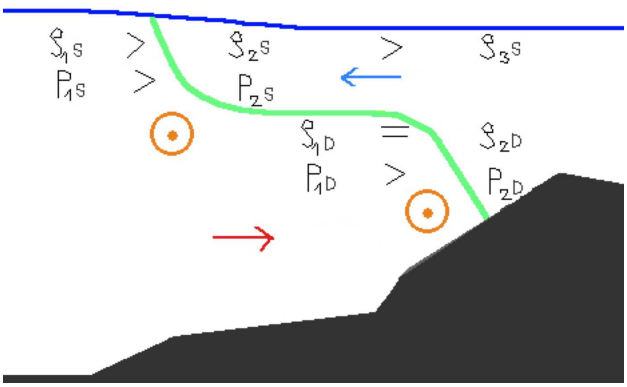

Figure 25: A schematic cross-frontal section explaining the southeastward geostrophic along-frontal jet with the two cores at the surface and deep expressions of the front. The blue and red arrows indicate the spreading of ArW and the submerging of AW, respectively, which presumably led to the formation of the surface and deep expressions of the front. Densities (ρ) and pressures (p) are labeled with S (surface front) and D (deep front). The border between AW (left) and ArW (right) is shown in green. The southwestern flank of the Great Bank is sketched in black and the sea surface in blue.

At depth, densities were nearly constant across the front due to thermohaline compensation. Nevertheless, a pressure gradient from the Atlantic to the Arctic side of the front must have been present to sustain the inner southeastward along-frontal core (right orange circle in Figure 25). The weak surface density gradient above the deep expression of the front (Figure 10) probably led to the pressure gradient that established the inner geostrophic core. SSH differences may further have been responsible for the pressure gradient at the deep expression of the front.

The width of the along-frontal current of 40-50 km agrees with findings in the southern BSPF (Berezut-

skii *et al.* , 1994). Each core had a width of about 15-20 km, corresponding to the distance of most pronounced hydrographic gradients in the surface and deep expressions of the front. This underlines the fact that the along-frontal cores were largely driven by the hydrographical structure of the BSPF.

Rotational effects explain why the pressure driven flow was isobaric with high pressure to the right, rather than down-gradient across the front (Coriolis, 1835; Cushman-Roisin, 1994). The internal Rossby radius of deformation ($R_i \approx 3$ km), indicates that rotational effects played an important role on scales larger than about 3 km in this study, which was also observed near the Spitzbergen Bank and in the northwestern Barents Sea during summer (Parsons *et al.* , 1996; Løyning, 2001).

Along-frontal flow in the BSPF - the Spitzbergen Bank versus the Great Bank

The southeastward along-frontal current and its dynamical explanation provided in the previous paragraph contrasts with the previously observed and modeled westward flow on the southern flank of the Spitzbergen Bank (Parsons *et al.* , 1996; Gawarkiewicz & Plueddemann, 1995). Westward flow on the southern flank of the Spitzbergen Bank may be driven by seasonal sea level differences between the Spitzbergen Bank and the southeastern Barents Sea (Li & McClimans, 1998). Additionally, the influence of the recirculatory AW on the southern flank of the Spitzbergen Bank and the southwestward flow of ArW on the Spitzbergen Bank (Loeng, 1991) might also support a southwestward frontal circulation along the flank of Spitzbergen Bank. Moreover, satellite altimetry indicates that the average sea surface height on the Spitzbergen Bank between 1995 and 1999 was higher than in most other parts of the Barents Sea (Peacock & Laxon, 2004). This suggests that different dynamics may govern the frontal circulation at the southern flank of the Spitzbergen Bank compared to the Great Bank. On the other hand, northeastward currents were also observed on the southern flank of the Spitzbergen Bank between the 150 and 250 m isobaths (Gawarkiewicz & Plueddemann, 1995), which agrees with the along-frontal flow direction found in the present study. Also, the topography in the present study did not extend below the 300 m isobath, whereas most westward flow was observed between 250 and 400 m on the southern flank of the Spitzbergen Bank (Parsons *et al.* , 1996). A direct comparison between the currents at the Great Bank and the Spitzbergen Bank is therefore difficult. Furthermore, observations by Johansen *et al.* (1988) indicate a fluctuating northeastward AW current along the slope of the Spitzbergen Bank, in agreement with the major southeastward flow direction observed in the present study. Laboratory models also suggest that a warm-core AW jet on the southeastern slope of the Spitzbergen Bank should exist, flowing northeastward towards the 250 m sill between the Great Bank and the Central Bank (McClimans & Nilsen, 1993; Li & McClimans, 1998; Slagstad & McClimans, 2005). Li & McClimans (1998) conclude that the current along the Spitzbergen Bank is predominately flowing in the northeastward direction. This is in agreement with the BSPF flow in this study, but contradicts the ob-

servations by Parsons *et al.* (1996) and the model by Gawarkiewicz & Plueddemann (1995). Clearly, the along-frontal circulation is too complex to be predicted by simplified models, and seasonal variability in sea level differences appears to influence the flow direction. Temporal variability of the currents in the Barents Sea has been measured before by Argos buoys (Loeng *et al.* , 1989). Therefore, additional direct current measurements along the flank of the Spitzbergen Bank, the Great Bank and the Central Bank are necessary to construct a more consistent theory of the along-frontal circulation in the BSPF.

Meanders and eddies

The cross-track velocity components were often non-zero, indicating that the along-frontal circulation was not strictly parallel to the along-frontal sampling sections (Figure 18). This was confirmed by a meandering streamline velocity field, which tended to flow along the salinity and temperature gradients close to the surface. Flow instabilities caused by horizontal velocity shear typically lead to shedding of eddies from a meandering flow (Cushman-Roisin, 1994). The difference between the velocities of the inner and outer cores of the along-frontal jet may therefore have caused eddies in the study area. An eddy may have been present in section 22, where the cores of fresh and cold water around the northeastern end of the HRSV were accompanied by doming isopycnals. Circular flow also emerged in the streamline function in the vicinity of the doming isopycnals in section 22, but not precisely at the same location. Since the hydrographic data did not extend deep enough to reveal a typical eddy signal, i.e. deepening isopycnals below the doming isopycnals in section 22, it can, however, not be concluded that this feature was an eddy. On scales larger than the HRSV, eddies are expected and have indeed been observed in the BSPF (Berezutskii *et al.* , 1994). Together with ageostrophic processes, eddies are important for cross-frontal exchange and vertical flow (Cushman-Roisin, 1994).

Finally, occurrences of anti-cyclonic eddies resulting from the local topography have been suggested in the vicinity of the Central Bank and the Great Bank (Loeng, 1991; Ingvaldsen & Loeng, 2009). The southeastward along-frontal flow observed in this study contradicts the notion of such an anti-cyclonic circulation around the Great Bank.

Ageostrophic components

In contrast to the strong influence of tides on the circulation in the western Barents Sea, they were negligible in this study. The small influence of tidal currents in the study region southwest of the Great Bank reduced the potential lateral distortion of the front due to tidal oscillation and subsequent aliasing problems (Gawarkiewicz & Plueddemann, 1995; Parsons *et al.* , 1996). However, when comparing the measured currents to the computed geostrophic currents, the geostrophic currents tended to be larger in magnitude, suggesting that ageostrophic processes other than tides decelerated the flow.

The weaker measured velocities of the inner core compared to the computed geostrophic velocities were probably caused to some extent by bottom friction. Bottom friction was expected to have a larger influ-

ence on the inner core than on the outer core, because the inner core was located at the steepest part of the bathymetry in the study region. This likely resulted in a larger interface between the bottom and the current at the inner core.

Parts of the outer core appeared to have merged with the inner core between sections 20 and 22 (downstream), since both the measured velocities and the computed geostrophic velocities indicated an increase in strength of the inner core between these sections, while the outer core weakened. As a consequence, horizontal velocity shear between the two cores must have been greater in section 22 than in section 20. This could explain the more disturbed salinity and temperature fields as well as the counter current observed between the two cores in section 22 (Figure 11 and 17). Also, the velocity difference between the computed geostrophic inner core and the measured inner core in section 22 was larger compared to section 20. This indicates that ageostrophic processes were stronger in section 22 than in section 20, which could explain the more oscillating isopycnals in section 22. The wave-shaped isopycnals may indicate that internal waves were present on the interphase between the relatively fresh surface layer and the submerged AW. This could further have decelerated the flow.

Ageostrophic processes are known to increase turbulence (Cushman-Roisin, 1994). The temporal difference of about 2 hours between each of the short sections may therefore have been sufficient for the flow to change significantly. The different measured directions of the flow in neighboring sections (Figure 19) may be an indication for such short-term variability. Hence, the sampling time may not have been short enough to obtain a synoptic image of the front. The slight mismatch between the observed currents and the computed, non-divergent streamline flow could consequently be explained by the attempt of fitting a synoptic streamline function onto slightly asynoptic current measurements.

Mixing processes and water mass formation

The Great Bank is an area of mixing and local water mass formation in the Barents Sea (Løyning, 2001). The sub-mesoscale water parcels and the small-scale hydrographic patches found in the high-resolution survey manifest a dynamic mixing zone in the BSPF near the Great Bank. Cross-frontal currents and turbulence that were indicated in this study were probably crucial for mixing in the frontal zone. The patchy hydrographic structure in the surface expression of the front suggests that AW and ArW was transported to the center of the front by cross-frontal currents. The observed zig-zag patterns in the TS-profiles (Figure 15) support this hypothesis. Lateral flows could have arisen from diffusion of heat and salt across the front (thermohaline intrusions, May & Kelley, 2002), or from velocity shear between the two main cores of the along-frontal jet. These cross-frontal processes probably mixed the distinct water parcels, until new PFW was eventually formed.

Wind may also have been a mixing force, as it opposed the major southeastward flow during the survey. The mixed layer was approximately 10 m deeper on the Atlantic side of the front. This was also observed on the southeastern slope of the Spitzbergen Bank,

and can be explained by increased wind mixing ability in more weakly stratified water (Parsons *et al.* , 1996).

AW, ArW and PFW, as defined by Loeng (1991) and Hopkins (1991), were detected in this study, but their definitions did not encompass all water masses observed in this survey. The most likely reason for this is surface heating of the upper water column, as water in the center and on the Arctic side of the surface front tended to be within the salinity range of the ArW and the PFW definitions, while the temperatures often exceeded the defined ranges. Summer heating may have been particularly strong in 2007. The temperatures of the Barents Sea in 2007 were generally close to those observed in 2006, which was the warmest year ever recorded in the Barents Sea (Hughes *et al.* , 2008). Near the Great Bank, temperatures deviated from the long term mean (1971-2000) by about plus one standard deviation. It is therefore likely that the unclassified water masses were influenced by radiative heating, which is an important transformation factor near the BSPF during summer (Harris *et al.* , 1998).

The cold temperatures below 60 m on the Atlantic side of the front were lower than the definitions for AW temperatures, while the salinity was close to 35 psu at all depths on the Atlantic side, which was within the range of the AW definitions. The coldest water on the Atlantic side of the front was found along the southeastern slope of the Great Bank, as already observed in the summer of 1996 (Løyning, 2001). This cold and saline bottom layer could have been formed on top of the Great Bank through cooling and salinization during the previous fall and winter, before sinking into the Hopen Deep. Since water on top of the Great Bank appears to be relatively stationary, sinking of cold and saline water along the slope of the Great Bank may happen throughout the summer (Løyning, 2001).

The ice-edge must have been relatively far north of the study site, since melt water with salinities below 34.2 psu was not observed. This contrasts summer observations from the southern flank of the Spitzbergen Bank, where significant amounts of low salinity surface water crossed the BSPF towards the Atlantic side during the early 1990s (Harris *et al.* , 1998). No dynamical explanation was provided for this cross-frontal exchange. Ageostrophic processes such as velocity shear and wind forcing stimulate cross-frontal exchange in the Polar Front west of Spitzbergen (Saloranta & Svendsen, 2001). Secondary frontal circulation, which appears to have been caused by instabilities arising from the horizontal velocity shear between the two cores of the BSPF and from bottom friction, as well as thermohaline intrusions, are suggested mechanisms from this study inducing cross-frontal exchange in the Barents Sea.

4.3 Physical-biological interactions in the BSPF

Fluorescence is a reasonable, though imperfect, measure of the phytoplankton standing crop (Miller, 2004). The observed fluorescence maximum on the Atlantic side of the front can therefore be interpreted as an ongoing phytoplankton bloom, while the weaker fluorescence maxima on the Arctic side represent smaller phytoplankton patches.

Bloom conditions on the Atlantic and Arctic side of the Polar Front

In the spring, light is limiting for the phytoplankton growth in the Barent Sea (Sakshaug *et al.* , 2009). North of the BSPF near the ice-edge, the spring bloom starts in April due to strong ice-melt and subsequent surface stratification, which retains the phytoplankton in the light-flooded euphotic zone (Sverdrup, 1953; Signorini & McClain, 2009). The strong pycnocline lasts throughout the summer and prevents exchange of nutrients, leading to a situation where nutrients become limiting instead of light. After an abrupt cessation of the bloom due to nutrient depletion, a thin layer of phytoplankton typically prevails near the pycnocline throughout the summer season (Sakshaug & Slagstad, 1992; Sakshaug *et al.* , 2009; Signorini & McClain, 2009). This scenario is consistent with the strong pycnocline found on the Arctic side of the front and the subsurface fluorescence maxima observed there in August 2007. Hence, the Arctic side of the BSPF was probably in a post-bloom condition.

In the permanently ice-free AW, stratification is weaker and mainly caused by summer heating (Wassmann *et al.* , 2006; Sakshaug *et al.* , 2009). This agrees with the weaker pycnocline that was observed on the Atlantic side of the front below the warm surface layer in August 2007. Due to late surface stratification, phytoplankton typically bloom in May or June south of the BSPF, followed by a period of low primary production in the summer due to nutrient limitation (Sakshaug & Slagstad, 1992; Wassmann *et al.* , 1999; Wassmann *et al.* , 2006; Basedow *et al.* , 2009; Norrbin *et al.* , 2009). This scenario contradicts the bloom observed on the Atlantic side of the BSPF in August. However, the general picture outlined above is thought to be obscured by oceanographic mesoscale variability and strong wind events (Wassmann *et al.* , 1999; Wassmann *et al.* , 2006). Model studies suggest that wind can trigger secondary blooms in the course of the summer in the southern Barents Sea by intermittently eroding the weak pycnocline (Sakshaug & Slagstad, 1992; Sakshaug *et al.* , 2009). This causes efficient upward transport of nutrient-rich water, stimulating primary production. The surface fluorescence maximum on the Atlantic side of the front observed in this study could therefore be a secondary bloom stimulated by wind mixing. In addition to wind mixing, the shoaling of the isopycnals on the Atlantic side of the surface front probably facilitated upwelling of nutrients to the euphotic zone. This could potentially have prolonged the observed bloom on the Atlantic side. It has been observed that plankton patches are often located at fronts because of along-isopycnal upwelling of nutrients (Nagai *et al.* , 2008), which would support the hypothesis of a longer integrated blooming period on the Atlantic side compared to the Arctic side. However, nutrient measurements are lacking to confirm this upwelling and mixing induced blooming hypothesis. Alternatively, the observed bloom could have been a coccolithophorid bloom. These frequently occur in the Barents Sea between July and September in waters that have recently been depleted by nutrients (Signorini & McClain, 2009). As phytoplankton samples are missing, the nature of the bloom observed on the Atlantic side of the front cannot be determined conclusively.

Peak abundances of copepods, which usually dominate the zooplankton community in the Barents Sea, typically occur in July (Eiane & Tande, 2009). The low zooplankton abundances on the Atlantic side of the front could therefore indicate that a significant amount of the zooplankton had already migrated to deeper water for over-wintering. This is consistent with the vertical distribution of zooplankton observed south of the BSPF near the Central Bank in July 1999, which suggested descent to depth at that time (Arashkevich *et al.* , 2002). The observed zooplankton on the Arctic side of the surface front likely belonged to a different community, since the BSPF separates copepod species dwelling in AW from species dominating in ArW (Melle & Skjoldal, 1998; Eiane & Tande, 2009). Nevertheless, due to the proximity of the zooplankton to the surface expression of the front, cross-frontal currents may have exchanged patches of different plankton communities across the front.

Causes of plankton patchiness

Plankton distributions in the ocean are known to be patchy and temporal. Also in the Barents Sea, zooplankton variability on small temporal and spatial scales has been observed (Helle, 2000; Tande *et al.* , 2000; Arashkevich *et al.* , 2002). Dispersive and cohesive physical and biological factors have been suggested to contribute to small-scale plankton aggregations (Huntley & Niiler, 1995; Zhou & Huntley, 1996; Mann & Lazier, 2006). The patchy hydrographic structure that was reflected in the structure of plankton patches in this study suggests that physical mechanisms were more important to form the plankton patches than biological factors.

Turbulent advection can transform large-scale variation in plankton distributions to small-scale variations with length scales of a few kilometers, such as those observed in the present study (Abraham, 1998). Hence, as for the water mass parcels, turbulent flow probably contributed to the formation of plankton patches in the frontal zone.

Phytoplankton patches were often found within patches of AW in the upper 20 m, suggesting that phytoplankton was advected from the ongoing bloom on the Atlantic side towards the center of the front by cross-frontal currents. Phytoplankton was also often confined between the density contours (e.g. Figure 21), further stressing the influence of hydrography on its distribution. This is consistent with the physical control on the phytoplankton distribution in other areas around Svalbard (Norrbin *et al.* , 2009).

From the zooplankton distribution in sections 20 and 22, it appears that zooplankton was influenced by the presence of the two along-frontal cores. Increased zooplankton abundances were observed in the upper parts of the cores, which could be explained by retention of the zooplankton in the strong currents. Water masses are further important for zooplankton distributions. On a relatively large scale, this has been observed in the waters north of Svalbard (Daase & Eiane, 2007), while a correlation between small-scale hydrographic and planktonic structures was observed in the Subantarctic Front off the coast of South Africa (Read *et al.* , 2002). In the present study, zooplankton patches often coincided with patches of AW in the upper 20 m, while between 20 and 50 m, zooplankton

abundances were highest in cool and relatively fresh water parcels. This supports the hypothesis that different zooplankton communities were present at different depths and parts of the HRSV, with species dominating in the AW near the surface on the Atlantic side of the front, and ArW dwelling species at greater depths and further northeast.

Due to their ability to move vertically in the water column, Arctic species may actively have entered parcels of AW to graze on phytoplankton. Hence, in addition to hydrographic constraints, the zooplankton patches may partly be explained by zooplankton behavior. This was also observed in other areas around Svalbard, where the zooplankton distribution was influenced by biological parameters (Norrbin *et al.* , 2009). The isolated areas of relatively low fluorescence coinciding with areas of high zooplankton abundances on the Atlantic side of the front may support the grazing hypothesis. On the other hand, these isolated areas had relatively low salinities compared to the surroundings, which suggests that dilution of phytoplankton rich AW with phytoplankton-poor ArW was at least partially responsible for the low fluorescence in these areas.

4.4 Future prospectives

Even though over large scales, ocean currents are two-dimensional, vertical flows form an important third dimension in frontal areas (Mahadevan, 2006). Since vertical motion is important for nutrient upwelling and water mass formation through mixing, vertical currents should be estimated for the BSPF to get a more complete understanding of its dynamics. Unfortunately, the weak vertical flow is difficult to measure due to insufficient accuracy of the ADCP instruments. Therefore, data assimilation models or indirect derivations using quasi-geostrophic equations are required to estimate vertical currents (Rixen *et al.* , 2003b). This was beyond the scope of the present study, but may be done as a follow-up study. Also, this study emphasized the analysis of the physical structure and dynamics of the BSPF, while the physical-biological interactions taking place in the BPSF were conspicuous and deserve further investigation. Statistical analyses on the influence of the physical and biological parameters on the plankton distributions is a suggested study continuation.

5 Conclusions

A high-resolution survey of the physical and biological structure of the BSPF near the Great Bank was conducted in August 2007. The following conclusions are derived from the results:

Physical properties of the BSPF near the Great Bank

- The hydrographic mesoscale structure of the BSPF on the southwestern flank of Great Bank is similar to that previously observed on the southern flank of the Spitzbergen Bank (Johannessen & Foster, 1978; Gawarkiewicz & Plueddemann, 1995; Parsons *et al.* , 1996; Harris *et al.* , 1998). A surface and a deep expression of the front, stronger stratification on the Arctic side

of the front and thermohaline compensation at depth are the most conspicuous hydrographic mesoscale characteristics of the BSPF.

- The dominant circulation in the BSPF near the Great Bank is a southeasterly geostrophic along-frontal jet. This indicates that the main flow directions along the BSPF can differ between the western Barents Sea and the Great Bank (Parsons *et al.* , 1996). Seasonal variability may explain these differences (Li & McClimans, 1998), but further investigations are required to gain a more complete understanding of the dynamics driving the along-frontal circulation.

- A quantitative mismatch between the computed geostrophic velocities and the observed velocity field indicates that ageostrophic processes retard the frontal circulation. Ageostrophic processes are therefore important for the overall circulation in the BSPF.

- It is suggested that water mass parcels from both sides of the front mix via turbulent stirring. Horizontal velocity shear between the the two cores of the along-frontal jet and between the cores and the ambient water, bottom friction as well as thermohaline intrusions are suggested ageostrophic processes that stimulate turbulence and cross-frontal flow in the BSPF.

- Variability in the sub-mesoscale structure and dynamics of the BSPF was presented in this study that former surveys were not capable of resolving. This includes a double core of the along-frontal jet associated with the surface and deep expressions of the front, hydrographic small-scale patches in the frontal zone with a length scale below 2 km and short term variability in the velocity field. Therefore, when planning future field programs to study the BSPF, small spatial and temporal scales should be considered.

Physical-biological interactions in the BSPF near the Great Bank

- Sub-surface fluorescence maxima near the pycnocline on the Arctic side of the BSPF suggest a post-bloom condition in August 2007.

- Shoaling isopycnals in the frontal zone and a weaker pycnocline with facilitated nutrient upwelling through wind mixing probably permitted the secondary phytoplankton bloom on the Atlantic side of the front in August 2007.

- Plankton patchiness is strongly developed near the BSPF. Physical processes such as isopycnal constraints, water mass dependence and turbulent stirring seem to be the dominant controlling factors of this biological small-scale variability.

- Small-scale plankton dynamics such as those found in this study are important for productivity on a large scale (Brentnall *et al.* , 2003). Additional high-resolution surveys of plankton distributions are therefore important to simulate the ecosystem of the Barents Sea more accurately in the future.

Acknowledgments

Project NESSAR was financed by the Norwegian Research Council IPY program. I thank my adviser Kurt Steinar Tande (Bodø University College) and my coadvisers Sünnje Linnéa Basedow (University of Tromsø) and Meng Zhou (University of Massachusetts Boston) for their editorial suggestions, advise and encouragement during the past year. Stimulating discussions took place with Frank Gaardsted (University of Tromsø) and Daniel Torres (Woods Hole Oceanographic Institution) during the data analysis period. Highly appreciated are also the chats and cake servings with my office mates Ingrid Wiedmann, Magnus Aune-Wiedmann and Kristine Hopland Sperre, which contributed to a very enjoyable stay at the University of Tromsø. Last but not least, I am deeply grateful to my husband Kjetil Våge (University of Bergen) for his invaluable personal support and professional advise.

References

Abraham, E. R. 1998. The generation of plankton patchiness by turbulent stirring. *Nature*, **391**, 577–580.

Arashkevich, E., Wassmann, P., Pasternak, A., & Riser, C. W. 2002. Seasonal and spatial changes in biomass, structure, and development progress of the zooplankton community in the Barents Sea. *Journal of Marine Systems*, **38**, 125–145.

Basedow, S. L., Tande, K. S., & Zhou, M. 2009. Biovolume spectrum theories applied: spatial patterns of trophic levels within a mesozooplankton community at the polar front. *Journal of Plankton Research*, **00**(0), 1–15.

Berezutskii, A. V., Maximov, S. E., Rogionov, V. G., & Sklyarov, V. E. 1994. Combined hydrologic and acoustic study of the polar front in the Barents Sea by contact and remote sensing techniques. *Oceanology*, **34**(1), 32–36.

Brentnall, S. J., Richards, K. J., Brindley, J., & Murphy, E. 2003. Plankton patchiness and its effect on larger-scale productivity. *Journal of Plankton Research*, **25**(2), 121–140.

Bretherton, F. P., Davis, R. E., & Fandry, C. B. 1976. A technique for objective analysis and design of oceanographic experiments applied to MODE-73. *Deep-Sea Research*, **23**, 559–582.

Coriolis, G. G. 1835. Memoire sur les équations du mouvement relatif des systèmes de corps. *Journal de l'école polytechnique*, **15**, 142–154.

Cushman-Roisin, B. 1994. *Introduction to Geophysical Fluid Dynamics*. Upper Saddle River, New Jersey 07458, USA: Prentice Hall.

Daase, M., & Eiane, K. 2007. Mesozooplankton distribution in northern Svalbard waters in relation to hydrography. *Polar Biology*, **30**, 969–981.

Dalpadado, P., & Bogstad, B. 2004. Diet of juvenile cod (age 0-2) in the Barents Sea in relation to food availability and cod growth. *Polar Biology*, **27**, 140–154.

D'Ericco, J. 2006. *Matlab Central - Surface fitting using gridfit.* `www.mathworks.com/matlabcentral/fileexchange/8998`.

Dorland, R. D., & Zhou, M. 2008. Circulation and heat fluxes during the austral fall in George VI Sound, Antarctic Peninsula. *Deep-Sea Research Part ii*, **55**, 294–308.

Eiane, K., & Tande, K. S. 2009. *Meso- and macrozooplankton.* In: Sakshaug, E., Johnsen, G. & K. Kovacs (Eds.), Ecosystem Barents Sea. Trondheim, Norway: Tapir Academic Press. Chap. 8, pages 209–234.

Ellingsen, I. H., Dalpadado, P., Slagstad, D., & Loeng, H. 2008. Impact of climatic change on the biological production in the Barents Sea. *Climatic Change*, **87**(155-175).

Emery, W. J., & Thomson, R. E. 2004. *Data analysis methods in physical oceanography.* Second edn. Amsterdam, The Netherlands: Elsevier.

Fanning, A., & Weaer, A. 1997. A horizontal resolution and parameter sensitivity study of heat transport in an idealized coupled climate model. *Journal of Climate*, **10**, 2469–2478.

Fong, D. A., & Monismith, S. G. 2004. Evaluation of the accuracy of a ship-mounted, bottom-tracking ADCP in a near-short coastal flow. *Journal of Atmospheric and Oceanic Technology*, **21**(7), 1121–1128.

Furevik, T. 2001. Annual and interannual variability of Atlantic Water temperatures in the Norwegian and Barents Seas: 1980-1996. *Deep-Sea Research Part I*, **48**(2), 383–404.

Garcia, V. M. T., Garcia, C. A. E., Mata, M. M., Pollery, R. C., Piola, A. R., Signorini, S. R., McClain, C. R., & Iglesias-Rodriguez, D. M. 2008. Environmental factors controlling the phytoplankton blooms at the Patagonia shelf-break in spring. *Deep-Sea Research Part I*, **55**(9), 1150–1166.

Gawarkiewicz, G., & Plueddemann, A. J. 1995. Topographic control of thermohaline frontal structure in the Barents Sea Polar Front on the south flank of Spitsbergen Bank. *Journal of Geophysical Reserach*, **100**(C3), 4509–4524.

Hansen, C., & Samuelsen, A. 2009. Influence of horizontal model grid resolution on the simulated primary production in an embedded primary production model in the Norwegian Sea. *Journal of Marine Systems*, **75**, 236–244.

Harris, C. L., Plueddemann, A. J., & Gawarkiewicz, G. G. 1998. Water mass distribution and Polar Front structure in the western Barents Sea. *Journal of Geophysical Reserach*, **103**(C2), 2905–2917.

Helland-Hansen, B., & Nansen, F. 1909. *The Norwegian Sea - Its physical oceanogrpahy based upon the Norwegian Researches 1900 - 1904.* Kristiania (Oslo): Det Mallingske Bogtrykkeri.

Helle, K. 2000. Distribution of the copepodite stages of *Calanus finmarchicus* from the Lofoten to the

Barents Sea in July 1989. *ICES Journal of Marine Science*, **57**, 1636–1644.

Herman, A. W., Beanlands, B., & Phillips, E. F. 2004. The next generation of Optical Plankton Counter: the Laser-OPC. *Journal of Plankton Research*, **26**(10), 1135–1145.

Hopkins, T. S. 1991. The GIN Sea - A synthesis of its physical oceanography and literature review 1972-1985. *Earth-Science Reviews*, **30**, 175–318.

Hughes, S. L., Holliday, N. P., & Beszczynska-Möller, A. 2008. ICES Report on Ocean Climate 2007. *ICES Cooperative Reserach Report*, 64 pp.

Huntley, M. E., & Niiler, P. P. 1995. Physical control of population dynamics in the Southern Ocean. *ICES Journal of Marine Science*, **52**, 457–468.

Ingvaldsen, R., & Loeng, H. 2009. *Physical oceanography.* In: Sakshaug, E., Johnsen, G. & K. Kovacs (Eds.), Ecosystem Barents Sea. Trondheim, Norway: Tapir Academic Press. Chap. 2, pages 33–64.

Ingvaldsen, R., Loeng, H., & Asplin, L. 2002. Variability in the Atlantic inflow to the Barents Sea based on a one-year time series from moored current meters. *Continental Shelf Research*, **22**, 505–519.

Ingvaldsen, R. B. 2005. Width of the North Cape Current and location of the Polar Front in the western Barents Sea. *Geophysical Research Letters*, **32**(L16603), doi:10.1029/2005GL023440.

Johannessen, O. M., & Foster, L. A. 1978. A Note on the topographically controlled oceanic Polar Front in the Barents Sea. *Journal of Geophysical Reserach*, **83**(C9), 4567–4571.

Johannessen, O. M., Good, D., & Smallenburger, C. 1977. Observation of an oceanic front in the Ionian Sea during early winter 1970. *Journal of Geophysical Reserach*, **82**(9), 1381–1391.

Johansen, G. O. 2002. Temporal and spatial variation in predation of juvenile herring (*Clupea harengus* L.) by Northeast Arctic cod (*Gadus morhua* L.) in the Barents Sea in 1984-1997. *ICES Journal of Marine Science*, **59**, 270–292.

Johansen, Ø., Mathisen, J. P., & Steinbakke, P. 1988. Environmental data collection in the Barents Sea. *Oceanor*, **Rep. OCN 88059**.

Kowalik, Z., & Proshutinsky, A. Y. 1995. Topographic enhancement of tidal motion in the western Barents Sea. *Journal of Geophysical Reserach*, **100**(C2), 2613–2637.

Li, S., & McClimans, T. A. 1998. The effects of winds over a barotropic retrograde slope current. *Continental Shelf Research*, **18**, 457–485.

Loeng, H. 1991. Features of the physical oceanographic conditions of the Barents Sea. *Polar Research*, **10**(1), 5–18.

Loeng, H., & Drinkwater, K. 2007. An overview of the ecosystems of the Barents and Norwegian Seas and their response to climate variability. *Deep-Sea Research Part II*, **54**, 2478–2500.

Loeng, H., Sundby, S., & Østensen, Ø. 1989. Drifting Argos buoys in the Barents Sea. *ICES CM Paper*, **C:19**, 1–10.

Loeng, H., Ozhigin, V., & Ådlandsvik, B. 1997. Water fluxes through the Barents Sea. *ICES Journal of Marine Science*, **54**, 310–317.

Løyning, T. B. 2001. Hydrography in the northwestern Barents Sea, July-August 1996. *Polar Research*, **20**(1), 1–12.

Mahadevan, A. 2006. Modeling vertical motion at ocean fronts: Are nonhydrostatic effects relevant at submesoscales? *Ocean Modelling*, **14**, 222–240.

Mann, K. H., & Lazier, J. R. N. 2006. *Dynamics of marine ecosystems: biological-physical interactions in the oceans*. 3rd edn. Oxford OX4 2DQ, UK: Blackwell Publishing.

May, B. D., & Kelley, D. E. 2002. Contrasting the interleaving in two baroclinic ocean fronts. *Dynamics of Atmospheres and Oceans*, **36**, 23–42.

McClimans, T. A., & Nilsen, J. H. 1993. Laboratory simulation of the ocean currents in the Barents Sea. *Dynamics of Atmospheres and Oceans*, **19**, 3–25.

Mehlum, F., Nordlund, N., & Isaksen, K. 1998. The importance of the "Polar Front" as a foraging habitat for guillemots *Uria* spp. breeding at Bjørnøya, Barents Sea. *Journal of Marine Systems*, **14**, 27–43.

Melle, W., & Skjoldal, H. R. 1998. Reproduction and development of *Calanus finmarchicus, C. glacialis* and *C. hyperboreus* in the Barents Sea. *Marine Ecology Progress Series*, **169**, 211–228.

Miller, C. B. 2004. *Biological Oceanography*. Malden, Massachusetts 02148, USA: Blackwell Publishing.

Morgan, P. P. 1994. *Seawater: A Library of Matlab Computational Routines for the Properties of Sea Water*. Tech. rept. CISRO Marine Laboratories.

Munch, A. T. 2008. *Polaråret - Alt kan skje i fronten*. `www.polararet.no/artikler/2008/1210933496.66`.

Nagai, T., Tandon, A., Gruber, N., & McWilliams, J. C. 2008. Biological and physical impacts of ageostrophic frontal circulations driven by confluent flow and vertical mixing. *Dynamics of Atmospheres and Oceans*, **45**, 229–251.

Nardelli, B. Buongiorno, Santoleri, R., & Sparnocchia, S. 2001. Small mesoscle features at a meandering upper-ocean front in the Western Ionian Sea (Mediterranean Sea): Vertical motion and potential vorticity analysis. *Journal of Physical Oceanography*, **31**, 2227–2250.

Norrbin, F., Eilertsen, H.C., & Degerlund, M. 2009. Vertical distribution of primary producers and zooplankton grazers during different phases of the Arctic spring bloom. *Deep-Sea Research Part II*, **56**, 1945–1958.

Padman, L., & Erofeeva, S. 2004. A barotropic inverse tidal model for the Arc-

tic Ocean. *Geophysical Research Letters*, **31**(L02303), doi:10.1029/2003GL019003.

Parsons, R., Bourke, R. H., Muench, R. D., Chiu, C.-S., Lynch, J. F., Miller, J. H., Plueddemann, A. J., & Pawlowicz, R. 1996. The Barents Sea Polar Front in summer. *Journal of Geophysical Reserach*, **101**(C6), 14201–14221.

Peacock, N. R., & Laxon, S. W. 2004. Sea surface height determination in the Arctic Ocean from ERS altimetry. *Journal of Geophysical Reserach*, **109**(C07001), doi:10.1029/2001JC001026.

Pedlosky, J. 1996. *Ocean Circulation Theory*. Berlin Heidelberg, Germany: Springer-Verlag.

Read, J. F., Pollard, R. T., & Bathmann, U. 2002. Physical and biological patchiness of an upper ocean transect from South Africa to the ice edge near the Greenwich Meridian. *Deep-Sea Research Part II*, **49**, 3713–3733.

Rixen, M., Allen, J. T., Alderson, S., Cornell, V., Crisp, N., Fielding, S., Mustard, A. T., Pollard, R. T., Popova, E. E., Smeed, D. A., & Srokosz, M. A. 2003a. Along or across front ocean survey strategy? An operational example at an unstable front. *Geophysical Research Letters*, **30**(1), 1017.

Rixen, M., Allen, J. T., & Pollard, R. T. 2003b. Along or across front ocean survey strategy? The estimation of quasi-geostrophic vertical velocities and temperature fluxes. *Geophysical Research Letters*, **30**(5), 1264.

Robinson, I. 2006. *SST: Observations of mesoscale ocean features*. `www.envisat.esa.int/Ocean2006/course_material/`.

Sakshaug, E. 1997. Biomass and productivity distribution and their variability in the Barents Sea. *ICES Journal of Marine Science*, **54**, 341–350.

Sakshaug, E., & Slagstad, D. 1992. Sea ice and wind: Effects on primary productivity in the Barents Sea. *Atmosphere-Ocean*, **30**(4), 579–591.

Sakshaug, E., Johnsen, G., Kristiansen, S., von Quillfeldt, C., Rey, F., Slagstad, D., & Thingstad, F. 2009. *Phytoplankton and primary production*. In: Sakshaug, E., Johnsen, G. & K. Kovacs (Eds.), Ecosystem Barents Sea. Trondheim, Norway: Tapir Academic Press. Chap. 7, pages 167–208.

Saloranta, T. M., & Svendsen, H. 2001. Across the Arctic front west of Spitzbergen: high-resolution CTD sections from 1998-2000. *Polar Research*, **20**(2), 177–184.

Signorini, S. R., & McClain, C. R. 2009. Environmental factors controlling the Barents Sea spring-summer phytoplankton blooms. *Geophysical Research Letters*, **36**(L10604), doi:10.1029/2009GL037695.

Skagseth, Ø. 2008. Recirculation of Atlantic Water in the western Barents Sea. *Geophysical Research Letters*, **35**(L11606), doi:10.1029/2008GL033785.

Slagstad, D., & McClimans, T. A. 2005. Modeling the ecosystem dynamics of the Barents Sea

including the marginal ice zone: I. Physical and chemical oceanography. *Journal of Marine Systems*, **58**, 1–18.

Sverdrup, H. U. 1953. On conditions for the vernal blooming of phytoplankton. *ICES Journal of Marine Science*, **18**, 287–295.

Tande, K. S., Drobysheva, S., Nesterova, V., Nilssen, E. M., Edvardsen, A., & Tereschenko, V. 2000. Patterns in the variations of copepod spring and summer abundance in the northeastern Norwegian Sea and the Barents Sea in cold and warm years during the 1980s and 1990s. *ICES Journal of Marine Science*, **57**, 1581–1591.

Trump, C. L., & Marmorino, G. O. 1998. Use of Single-Ping Bottom-Track ADCP data to characterize small-scale bathymetry. *Journal of Atmospheric and Oceanic Technology*, **15**, 299–303.

Trump, C. L., & Marmorino, G. O. 2002. Spatial processing of range-bin ADCP data to resolve small-scale frontal features. *Journal of Atmospheric and Oceanic Technology*, **19**(9), 1461–1468.

van Aken, H. M., Quadfasel, D., & Warpakowski, A. 1991. The Arctic Front in the Greenland Sea during February 1989: Hydrographic and biological observations. *Journal of Geophysical Reserach*, **96**(C3), 4739–4750.

Wassmann, P., Ratkova, T., Andreassen, I., Vernet, M., Pedersen, G., & Rey, F. 1999. Spring bloom development in the marginal ice zone and the central Barents Sea. *Marine Ecology*, **20**(3-4), 321–346.

Wassmann, P., Slagstad, D., Riser, C. W., & Reigstad, M. 2006. Modelling the ecosystem dynamics of the Barents Sea including the marginal ice zone II. Carbon flux and interannual variability. *Journal of Marine Systems*, **59**, 1–24.

Zhou, M., & Huntley, M. E. 1996. The principle of biological attraction, demonstrated by the biocontinuum theory of zooplankton patch dynamics. *Journal of Marine Research*, **54**, 1017–1037.